Research Article

Micromechanical characterization of microwave dielectric ceramic BaO–Sm$_2$O$_3$–5TiO$_2$ by indentation and scratch methods

Ming Liu[*], Zhitong Xu

Fujian Provincial Key Laboratory of Terahertz Functional Devices and Intelligent Sensing, School of Mechanical Engineering and Automation, Fuzhou University, Fuzhou 350108, China

Abstract: Mechanical characterization of dielectric ceramics, which have drawn extensive attention in wireless communication, remains challenging. The micromechanical properties with the microstructures of dielectric ceramic BaO–Sm$_2$O$_3$–5TiO$_2$ (BST) were assessed by nanoindentation, microhardness, and microscratch tests under different indenters, along with the X-ray diffraction (XRD), scanning electron microscopy (SEM), and Raman spectroscopy. Accurate determination of elastic modulus (E_{IT}) (i.e., 260 GPa) and indentation hardness (H_{IT}) (i.e., 16.2 GPa) of brittle BST ceramic by the instrumented indentation technique requires low loads with little indentation-induced damage. The elastic modulus and indentation hardness were analyzed by different methodologies such as energy-based approach, displacement-based approach, and elastic recovery of Knoop imprint. Consistent values (about 3.1 MPa·m$^{1/2}$) of fracture toughness (K_C) of BST ceramic were obtained by different methods such as the Vickers indenter-induced cracking method, energy-based nanoindentation approaches, and linear elastic fracture mechanics (LEFM)-based scratch approach with a spherical indenter, demonstrating successful applications of indentation and scratch methods in characterizing fracture properties of brittle solids. The deterioration of elastic modulus or indentation hardness with the increase in indentation load (F) is caused by indentation-induced damage and can be used to determine the fracture toughness of material by energy-based nanoindentation approaches, and the critical void volume fraction (f^*) is 0.27 (or 0.18) if elastic modulus (or indentation hardness) of the brittle BST ceramic is used. The fracture work at the critical load corresponding to the initial decrease in elastic modulus or indentation hardness can also be used to assess the fracture toughness of brittle solids, opening new venues of the application of nanoindentation test as a means to characterize the fracture toughness of brittle ceramics.

Keywords: brittle ceramics; micromechanical properties; instrumented indentation; microscratch; fracture toughness (K_C); grid nanoindentation

1 Introduction

The rapid development of wireless communication

* Corresponding author.
E-mail: mingliu@fzu.edu.cn

with the broadband network has significantly increased the demand for microwave dielectric ceramics of excellent dielectric behaviors (e.g., suitable relative permittivity, high quality factor ($Q \times f$), and low-temperature drift of resonance frequency [1–3]) together with high mechanical properties (e.g., elastic modulus (E_{IT}), hardness, and

fracture toughness (K_C) [4–7]), since excellent mechanical properties (e.g., high cracking resistance [8–11] and penetration resistance [12,13]) can ensure high structural stability, high reliability, and long-term service life of dielectric ceramics and have drawn extensive attention in the field of dielectric ceramics [4–6,14]. Values of Meyer hardness (H_{VM}) and Knoop hardness (H_K) of dielectric ceramic $(Ba_{0.9}Ca_{0.1})_{0.9}(Na_{0.5}Bi_{0.5})_{0.1}TiO_3$ were found to be almost the same, and both of them increased with the increasing sintering temperature [15]. The dielectric ceramics $Ba_{6-3x}R_{8+2x}Ti_{18}O_{54}$ ($0 \leqslant x \leqslant 1$, R denotes the rare-earth element such as Nd, Sm, La, and Pr) with tungsten bronze-type structure have been extensively applied to microwave devices due to their excellent microwave properties [16]. The micromechanical properties of dielectric ceramic $BaO–Sm_2O_3–5TiO_2$ (BST), which has excellent microwave properties (i.e., high permittivity of 77 and high $Q \times f$ of 9300 GHz) and good temperature stability of capacitance [17,18], have not been well characterized. Guo *et al.* [19] reported that the Al/Nd co-doping method can significantly improve the dielectric properties of microwave dielectric ceramic $Ba_4Nd_{9.33}Ti_{18}O_{54}$. Adamczyk *et al.* [20] found that the addition of vanadium can significantly enhance the mechanical properties (i.e., elastic modulus and indentation hardness (H_{IT})) of dielectric ceramic $BaBi_2(Nb_{0.99}V_{0.01})_2O_9$. Guiu *et al.* [21] reported that indentation-induced cracking of poled and unpoled piezoelectric materials by Vickers indenter strongly depended on the orientation of the poling direction. Fracture toughness of brittle dielectric materials has been widely characterized by the Vickers indenter-induced cracking method rather than conventional methods (e.g., three-point bending and pre-cracked single-edge V-notched beam methods [22,23]). Nevertheless, the Vickers indenter-induced cracking method has various expressions for radial cracking or median cracking [24], whose applicability and reliability remain examination.

Instrumental indentation (i.e., nanoindentation) that does not entail a complicated process of sample preparation has been widely used to characterize the micromechanical properties [25] (e.g., elastic modulus [26], bonding properties [27], tensile properties [28], creep behavior [29], low-cycle fatigue [30,31], residual stress [32], and fracture toughness [33,34]) of various materials (e.g., metals [35], glasses [36], metallic glasses [37], ceramics [7,38], polymers [39–41], piezoelectric materials [42–45], thin films [46–49], and composites [50]). The microscratch test is also an effective technique to investigate the scratch resistance of material [51], the structural integrity of multilayer coatings [52], tribological behavior [53,54], contact-induced damage/cracking [55], scratch-induced buckling failure of silicon nitride ceramic films [56], and the scratch behavior of Ce-doped yttrium aluminum garnet (YAG, $Y_3Al_5O_{12}$) coatings [57].

In the current work, the micromechanical properties of BST ceramic, whose microstructures were characterized by the X-ray diffraction (XRD), scanning electron microscopy (SEM) equipped with backscattered electron (BSE) imaging, and Raman spectroscopy, were estimated by various methods with the focus on comparison of different methodologies and their applicability to brittle ceramics: Elastic modulus and indentation hardness were estimated via the nanoindentation technique by the standardized Oliver and Pharr (OP) method that requires the area function of the indenter [56] and other methods that do not require calibration of the indenter such as c_2 method [57], Cheng theory [58–60], Gong theory [61,62], energy-based approach [59], and displacement-based approach [63]; elastic modulus was also calculated based on the elastic recovery of the imprint by Knoop indenter [64]; fracture toughness was evaluated by the Vickers indenter-induced cracking method that requires a large amount of measurements of crack length under many repeated tests; energy-based nanoindentation approaches [64,65] with Berkovich indenter can be used to characterize fracture toughness in the absence of surface cracking (or surface cracking is too slight to be accurately measured) based on the data under various indentation loads (F); and linear elastic fracture mechanics (LEFM)-based [66] or microscopic energetic size effect law (MESEL)-based [67–71] scratch approaches can also be used to assess fracture toughness, and one scratch test would suffice, since various loads can be progressively applied to a single scratch test. Consistent values of fracture toughness of BST ceramic can be obtained by different methods: The critical void volume fraction (f^*) used in energy-based nanoindentation approaches is found to depend on whether the deterioration elastic modulus or indentation hardness is used; the critical load at the initial decrease in elastic modulus or indentation hardness can be used to determine the fracture work for assessing fracture toughness of brittle solids; and LEFM-based scratch approach with a spherical indenter provides the most

convenient means to characterize fracture toughness of brittle ceramics. To the best of our knowledge, this work is the first to systematically compare various indentation-based or scratch-based methodologies of assessment of micromechanical properties (i.e., elastic modulus, hardness, and fracture toughness) of brittle ceramics and aims to provide the paradigm of micromechanical characterization of brittle solids by instrumented indentation and scratch technologies.

2　Experimental procedures and analysis approaches

2. 1　Experimental procedures of material preparation and characterization

The BST ceramic was synthesized by the solid-state reaction method with fine powders (regent grade, purity > 99.9 wt%; Sinopharm Chemical Reagent Co., Ltd., Shanghai, China) of $BaCO_3$, TiO_2, and Sm_2O_3 (nominal ratio of 20.9 : 42.2 : 36.9) [22]. The powder mixtures, which were wet ball-milled for 12 h in a nylon jar using deionized water and zirconia balls, were passed through an 80-mesh sieve after drying at 130 ℃ and calcined in an ambient atmosphere for 4 h at 1170 ℃ with a heating rate of 10 K/min in the muffle furnace, followed by natural air-cooling inside the furnace [18]. Then, the samples were formed by uniaxially pressing the powder mixtures into a cylindrical mold under the pressure of 180 MPa. BST specimens were prepared by sintering at 1350 ℃ for 4 h in the furnace at the heating rate of 3 K/min, followed by natural air-cooling inside the furnace. The surface of cylindrical BST ceramic sample (diameter of 12 mm and height of 6 mm) was ground and polished using SiC waterproof abrasive papers (different grits from 600# to 3000#) and commercially available diamond polishing paste (2.5# μ-grit), respectively. Then, the smooth surface of BST ceramic sample can be obtained after polishing by ion beams on an ion beam slope cutter (EM TIC 3X, Leica, Wetzlar, Germany), and the optical observations are shown in Fig. 1(b) and the inset of Fig. 2(a). The bulk density of BST was measured to be 5.5385 g/cm^3 by the gas displacement method on a pycnometer (AccuPyc II 1340, Micrometrics, Cumming, USA). The microstructure of BST ceramic was characterized by the XRD on an X-ray diffractometer

(Empyrean-DY1602, Manufacturer) with Cu Kα radiation (wavelength of 0.1542 nm, 2θ of 5°–90°, and scan step of 0.0131 (°)/s). The thermally etched microstructure (heating at 10 K/min up to 1240 ℃, dwelling for 1 h, followed by natural air-cooling inside the furnace) was observed with the SEM using a microscope (Quanta 250 FEG, FEI, Hillsboro, USA) and also characterized by the Raman spectroscopy on a Raman microscope (inVia Reflex, Renishaw, London, UK) with helium–neon ion laser excitation (electric power of 17 mW and wavelength of 532 nm).

The nanoindentation tests were carried out by a nanoindentation tester (NHT^2, Anton Paar, Graz, Austria) with diamond Berkovich indenter (loading/ unloading time of 5 s and dwelling time of 2 s for grid nanoindentation at indentation load of 3 mN; loading/ unloading time of 30 s and dwelling time of 10 s for nanoindentation under various loads) to investigate the micromechanical properties of BST ceramic. Time-dependent mechanical properties of the material required the application of a constant strain rate during the nanoindentation test [72,73], which was not used in the current study, since mechanical properties of brittle ceramics can be assumed to be time-independent, and a constant loading rate was used without considering the effect of strain rate. Moreover, a constant strain rate condition was more difficult to maintain than a constant loading rate condition, and the measurement by a constant loading rate was more accurate than that by a constant strain rate [39]. Berkovich indenter was the most commonly used and easily constructed, since the three edges of the triangular indenter can meet at a single point, while the four edges of the pyramid indenter (e.g., Vickers indenter and cube corner indenter) were very difficult to meet at a single point, resulting in the inevitable line for the four-sided pyramid indenters [72]. Elastic modulus of the machined cylindrical BST ceramic sample (4.23 mm in diameter and 5.28 mm in height, 0.41 g) was also measured by a resonant ultrasound spectroscope (Quasar, Albuquerque, USA).

The scratch response of BST ceramic was investigated using a microscratch tester (MST^2, Anton Paar, Graz, Austria) by either Berkovich (the sharp edge was along the scratch direction: edge-forward orientation) or spherical indenter with radius of 500 μm in the atmospheric environment [74–76] under progressively increasing normal load (F_n) (initial load of 5 mN) and scratching speed of 3 mm/min. Cracking was detected

by acoustic emission (AE) signals acquired by the passive Vallen piezoelectric AE sensor (Vallen, Munich, Germany) with a central frequency of 150 kHz, dynamic range of 65 dB_{AE}, and maximum amplification of 179,200, which can capture acoustic spikes (i.e., micro-movements of the sample due to waves generated by sudden events such as cracking) and convert their numbers to volts that are sent to the software. The AE sensitivity factor (C) (i.e., the number between 1 and 9), which multiplies the signal in volts received from the AE sensor, was set to 7, since a small sensitivity cannot monitor the initiation of small cracking, while a large sensitivity can introduce signal noise. For $C = 1$, the signal went without modification directly to the software. For a higher C, the value of AE signal (V_a) is $C \times V_i$, where V_i is the input signal, and the AE value ($= V_a/V_{max} \times 100\%$) corresponds to V_a divided by the maximum range (V_{max}) of 5 V. Since sample tile can affect scratch response [75,77], surface tilt angle was measured to be 0.15° by the pre-scan of the initial surface profile, resulting in negligible effect of sample tilt.

2. 2 OP method for analyzing instrumented indentation

The contact stiffness (S) is calculated at the beginning of the unloading segment (or the maximum displacement (h_{max})) of indentation load–displacement (F–h) curve, whose unloading part can be described by a power-law function [58]:

$$\frac{F}{F_{max}} = \left(\frac{h - h_p}{h_{max} - h_p}\right)^m, \quad S = \frac{dF}{dh}\bigg|_{h_{max}} = \frac{mF_{max}}{h_{max} - h_p} \quad (1)$$

where h is the indentation displacement; F_{max} is the maximum indentation load; and h_p, which is the permanent indentation displacement, and m, which is the fitting index in the range of 1.2–1.7 for most materials [39,64], are determined by fitting the unloading curve from 40% to 98% of F_{max}.

The reduced plane strain modulus (E_r) (i.e., the combined moduli of the sample and the indenter) and H_{IT} can be calculated from S:

$$\frac{1}{E_r} = \frac{1 - v^2}{E_{IT}} + \frac{1 - v_i^2}{E_i} = \frac{2\beta}{S}\sqrt{\frac{A_p(h_c)}{\pi}},$$

$$H_{IT} = \frac{F_{max}}{A_p(h_c)}, \quad h_c = h_{max} - \varepsilon\frac{F_{max}}{S} \quad (2)$$

where v ($= 0.2$) [7] is the Poisson's ratio of BST

ceramic; E_i ($= 1141$ GPa) and v_i ($= 0.07$) are elastic modulus and Poisson's ratio of the diamond indenter, respectively; β ($= 1.034$) is the correction factor for Berkovich indenter lacking axial symmetry [58]; the projected contact area (A_p) can be determined at h_{max}, and the contact area function ($A_p(h_c)$) is a function of contact depth (h_c); and ε is dependent on m [49,78]. The $A_p(h_c)$ of the indenter was obtained by performing nanoindentation tests on a standard material (i.e., fused silica) of known elastic modulus and Poisson's ratio under various loads ($\leqslant 100$ mN for fused silica in order to avoid cracking) with B-spline interpolation [58]. The $A_p(h_c)$ played a significate role in the OP method, whereas the rigorous methodology for precise determination of $A_p(h_c)$ still required evaluation and discussion, since $A_p(h_c)$, which was dependent not only on indenter geometry but also on material properties [78], was sensitive to many factors (e.g., pile-up, sink-in [79], pop-in [80], residual stress [80], surface effect [81], friction [82], and zero-point of initial contact [83]), and the significant uncertainty can be introduced when an area function pre-calibrated on a reference material was applied to calculate the A_p for other material of distinguished properties from the reference material [84].

3 Results and discussion

3. 1 Microstructure characterization

Figure 1(a) shows the XRD patterns of BST ceramic that has $Ba_{3.99}Sm_{9.34}Ti_{18}O_{54}$ phase of the orthorhombic tungsten bronze structure [18,85]. The lattice parameters (a_0, b_0, and c_0), theoretical density, and cell volume obtained by the Rietveld-based quantitative analysis are listed in Table 1: Three lattice parameters are different ($a_0 \neq b_0 \neq c_0$), and the angles between a_0, b_0, and c_0 are all 90° ($\alpha = \beta = \gamma = 90°$). The theoretical density of $Ba_{3.99}Sm_{9.34}Ti_{18}O_{54}$ (i.e., 5.8948 g/cm³) is larger than the density measured by the gas displacement method (i.e., 5.5385 g/cm³), resulting in the relative density of 5.5385/5.8948 = 94% owing to the porosity caused by the residual air when the sample was formed during preparation [86]. Figure 1(b) shows the optical microscopy image of BST polished by ion beams on an ion beam slope cutter (EM TIC 3X, Leica, Wetzlar, Germany) before thermal etching: The white and brown regions embedded in the grey substrate with randomly distributed pores can be observed on the
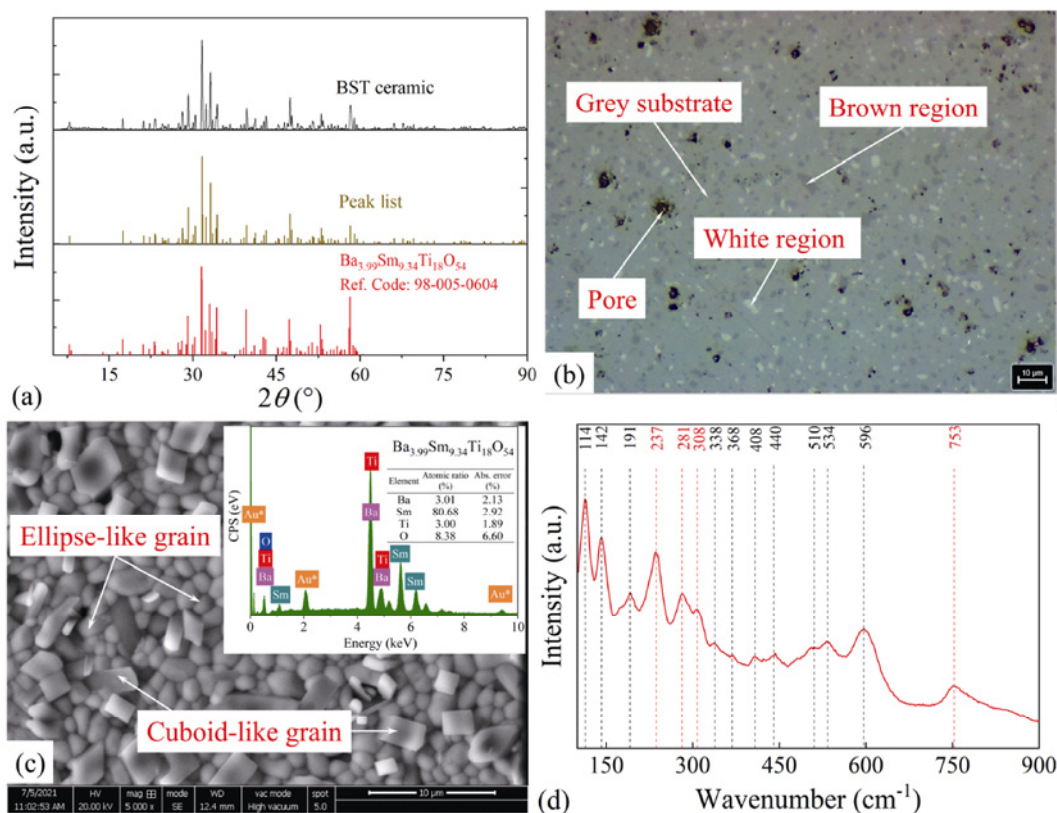
Fig. 1 Microstructure characterization of BST ceramic: (a) XRD patterns; (b) optical microscopy image before thermal etching with a Leica DVM6 digital microscope; (c) BSE image after thermal etching with the energy dispersive spectroscopy (EDS) spot analysis; and (d) laser micro-Raman spectroscopy spectrum of BST ceramic.

Table 1 a_0, b_0, and c_0 with theoretical density and cell volume of BST ceramic

Phase	Refined lattice (Å)			Theoretical density (g/cm³)	Cell volume (Å³)
	a_0	b_0	c_0		
$Ba_{3.99}Sm_{9.34}Ti_{18}O_{54}$	22.2972	7.6534	12.1472	5.8948	2072.9123

Note: α, β, and γ, which are angles between a_0, b_0, and c_0, are all 90°.

smooth surface after the final polishing by ion beams. The three different regions (i.e., white and brown regions with grey substrate) are caused by the different extents of crystallinity during sintering [87]. Although differently colored regions have different extents of crystallinity, they possess the same phase, and cannot be differentiated by the normal XRD analysis.

Figure 1(c) shows the dense and homogenous microstructure of thermally etched BST ceramic by BSE imaging. The grain sizes were measured by Image Pro Plus 6.0 software (the arithmetic average of 10 grains was reported): The mean size of the cuboid-like grains is 2.7 µm, which is about half of that of the ellipse-like grains (i.e., 5 µm). The elements measured by the EDS spot analysis are in agreement with the chemical compositions of BST ceramic, while the EDS

spot analysis can only provide evidence of elements, since the atomic ratios of elements (i.e., Ba, Sm, Ti, and O) cannot be accurately determined. Figure 1(d) shows that laser micro-Raman spectrum of BST ceramic consists of 15 well-resolved peaks centered at 114, 142, 191, 237, 281, 308, 338, 408, 440, 510, 534, 596, and 753 cm^{-1}. The peaks at 237 and 281 cm^{-1} are related to the tilt of oxygen octahedral; the peak near 308 cm^{-1} is associated with the tilt of the octahedral caused by the large empty cation sites; the peaks around 440 and 753 cm^{-1} are caused by lattice defects; the peaks centered at 596 cm^{-1} is associated with the symmetric stretching of the basal oxygen of the octahedral [88].

3.2 Grid nanoindentation

Figure 2(a) shows the indentation load–displacement curves for three different regions (i.e., grey substrate and brown and white regions) at F_{max} = 3 and 10 mN: The loading curves of the same colored region under two different F_{max} follow the same trace and show excellent reproducibility, since the nanoindentation tests were carried out on the central areas of three
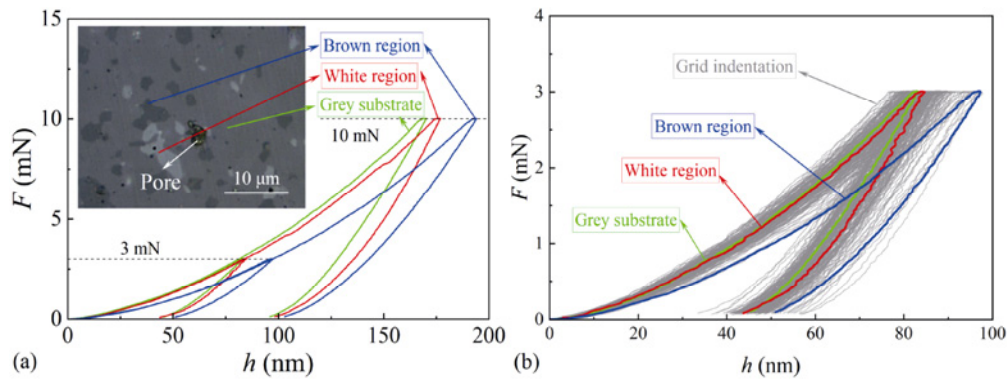
Fig. 2 Indentation load–displacement curves of three differently colored regions (i.e., grey substrate and brown and white regions) of dielectric BST ceramic: (a) at F_{max} =3 and 10 mN (the inset shows the grey, white, and brown regions that are clearly distinguished by the optical microscopy); (b) comparison between isolated nanoindentation and grid nanoindentation at F_{max} = 3 mN.

differently colored regions, which were not randomly selected, and the regions of the same color are expected to possess the same mechanical properties. Moreover, the locally tested regions were carefully chosen to avoid defects, and the indented areas were small without influence of surrounding material of different mechanical properties. The effect of surface roughness can be ignored, and the nanoindentation tests performed on the central areas of three differently colored regions, thanks to the accurate positioning of the state-of-the-art instrument, indicate the inhomogeneity of BST ceramic due to the non-uniform crystallinity. The maximum indentation displacements at F_{max} = 3 and 10 mN are smaller than 120 and 200 nm, respectively, resulting in sufficiently smaller indent lengths than the characteristic lengths of individual phases (or regions). The nanoindentation results of the three different regions (Fig. 2(a)) under F_{max} = 3 and 10 mN are compared in Table 2. The values of E_{IT} and H_{IT} of three different regions are approximately independent of load, indicating that the indents are sufficiently smaller than those of the individual phases under F_{max} = 3 mN. Therefore, the effect of the surrounding phases on the indentation response of the individual phase can be negligible. The grey substrate and brown region exhibit the smallest

Table 2　Nanoindentation results of three regions of BST ceramic at F_{max} = 3 mN

Region	E_{IT} (GPa)	h_{max} (nm)	W_e (nJ)	H_{IT} (GPa)	h_c (nm)	W_t (nJ)
Grey	**261** (264)	**84**	**49**	19.2 (17.4)	60	96
White	**267** (270)	**88**	**50**	**14.8** (14.1)	**70**	**102**
Brown	188 (190)	96	62	**14.3** (13.3)	**71**	**106**

Note: The values of E_{IT} and H_{IT} in parentheses were obtained at F_{max} = 10 mN. The bold values highlight the similarity between two different regions.

and largest h_{max}, respectively, indicating their greatest and weakest penetration resistance (or hardness), respectively. The grey substrate and the white region exhibit more or less the same E_{IT}, h_{max}, and elastic recovery work (W_e). The white and brown regions exhibit almost the same H_{IT}, h_c, and total deformation work (W_t).

Figure 2(b) shows the comparison of load–displacement curves at F_{max} = 3 mN between isolated nanoindentation on the preselected regions within the individual phases and grid nanoindentation (15 × 15 array) on randomly selected regions (inter-indent spacing = 10 μm). The scattering of nanoindentation data (Fig. 2(b)) is due to the influence of the surrounding material with different mechanical properties, since grid nanoindentation was carried out on randomly selected regions. The differently colored regions (the inset of Fig. 2(a)) are very small, and a small load (i.e., 3 mN) is required by grid nanoindentation. The majority of grid nanoindentation curves is located around the grey substrate and white region, indicating that the sum of grey substrate and white regions occupies the predominantly large fraction of volume with the brown regions only occupying a small fraction of volume. Although the isolated nanoindentation on the central area of an individual phase can be used to measure the mechanical properties of an individual phase of heterogeneous material under shallow indentation depth without influence of surrounding phases, grid nanoindentation is indispensable under the conditions that individual phases are invisible by the optical microscopy, etching can modify surface properties and increase surface roughness [89], and the effect of surrounding phases cannot be neglected. Moreover, both micromechanical properties (e.g., elastic modulus,

indentation hardness, creep [90], and fracture toughness [91]) and surface fractions of different phases of multi-phase materials [92] (e.g., α–β brass, cast iron, and Ti64–10TiC [89], electrode $LiNi_{0.5}Mn_{0.3}Co_{0.2}O_2$ [93], and shales [94–96]) can be obtained by statistically analyzing the nanoindentation results of grid tests on randomly selected regions. The surface fraction of an individual phase can be obtained under the assumption of Gaussian distribution of indentation parameters, and the surface fraction is equivalent to volume fraction by assuming random distribution of different phases in a three-dimensional spatial space [94]. Heterogeneous microstructures are widely observed in various materials (e.g., carbon steels, brasses, concretes, and rocks), and micromechanical properties of individual phases with their volume fractions determine the macroscopic performance of material and can be used as hints for material assessment and development, e.g., calcium-silicate-hydrate of two different phases (i.e., low and high densities) can be investigated by grid nanoindentation, and thus the effects of micromechanical properties and volume fractions of two phases on the macroscopic elasticity of the bulk material can be quantified [97,98]. Nevertheless, some challenges remain, and the initial fitting estimates, size of array, inter-indent spacing, and the effect of interface between particle and substrate (or particle) should be appropriately set [99]. The results (Table 2) obtained by isolated nanoindentation of individual phases are used as the initial non-linear fitting estimates. The normalized Gaussian probability density function (*f*) can be expressed as

$$f(x_i; c_i, \mu_i, \sigma_i^2) = \sum_{i=1}^{n} \frac{c_i}{\sqrt{2\pi}\sigma_i} \exp\left(-\frac{x_i - \mu_i}{2\sigma_i^2}\right),$$

$$\mu_i = \frac{1}{N_i} \sum_{k=1}^{N_i} x_k, \quad \sigma_i^2 = \frac{1}{N_i - 1} \sum_{k=1}^{N_i} (x_k - \mu_i) \quad (3)$$

where the subscript i is the serial number of the individual phase; n is the total number of phases that are represented by Gaussian peaks, N_i is the test number of phase i; x is the specific indentation parameter; μ and σ are the average value and standard deviation (SD) of x, respectively; and c_i is the mixing parameter (i.e., the weight of Gaussian peak) corresponding to the volume fraction of an individual phase. The normalized probability density function and c_i satisfy

$$\int_{-\infty}^{+\infty} f(x_i; c_i, \mu_i, \sigma_i^2)dx = 1, \quad \sum_{i=1}^{n} c_i = 1, \quad c_i \in \{0, 1\} \quad (4)$$

Figure 3 shows the normalized probability density plots of various indentation parameters obtained under F_{max} = 3 mN. Since the difference in mechanical properties among the three regions of BST ceramic is small (Table 2), the effect of phase boundary on the grid nanoindentation tests can be ignored [99]. Bimodal Gaussian distribution was adopted to fit the normalized probability density plots of E_{IT}, h_{max}, and W_e (Figs. 3(a)–3(c)), since the grey substrate and white region have close E_{IT}, h_{max}, and W_e and can be grouped to be one phase. Bimodal Gaussian distribution was used when analyzing H_{IT}, h_c, and W_t (Figs. 3(d)–3(f)), since the white and brown regions have close H_{IT}, h_c, and W_t and can be grouped to be one phase. The μ of predominant peaks (Fig. 3) are almost the same as those of grey substrate (Table 2), since the grey substrate occupies the largest volume fraction observed by the optical microscopy; while the μ of minority peaks are close to those of the brown region. The results of grid nanoindentation show that E_{IT} = 260 GPa, h_{max} = 84 nm, and W_e = 56 nJ for both the grey substrate and white region and E_{IT} = 190 GPa, h_{max} = 91 nm, and W_e = 50 nJ for the brown region, which are in good agreement with the results obtained on individual phases, as shown in Table 2.

The volume fractions of the three differently colored regions (i.e., grey substrate, white and brown regions) (Table 3) cannot be directly obtained by analyzing the normalized probability density plots of various indentation parameters with bimodal Gaussian fitting, resulting in the volume fraction of one colored region and the sum of volume fractions of the other two differently colored regions, as shown in Fig. 3. Consistent and reasonable indentation parameters and volume fractions of the three differently colored regions of the hard and brittle BST ceramic can be obtained by grid nanoindentation with bimodal Gaussian fitting and appropriately initial fitting estimates without considering the theoretical interface reported for a soft material [100]: Volume fraction (i.e., 8%) of brown region is obtained by statistical analysis of E_{IT}, h_{max}, and W_e with consistent results; volume fraction (i.e., about 84%) of grey substrate is obtained by statistical analysis of H_{IT}, h_c, and W_t with consistent results; the sum of volume fraction (i.e., about 16%) of white and brown regions is obtained by statistical analysis of H_{IT}, h_c, and W_t with consistent results, and thus volume fraction of white region can be calculated to be 8%, which is the same as that of brown region.
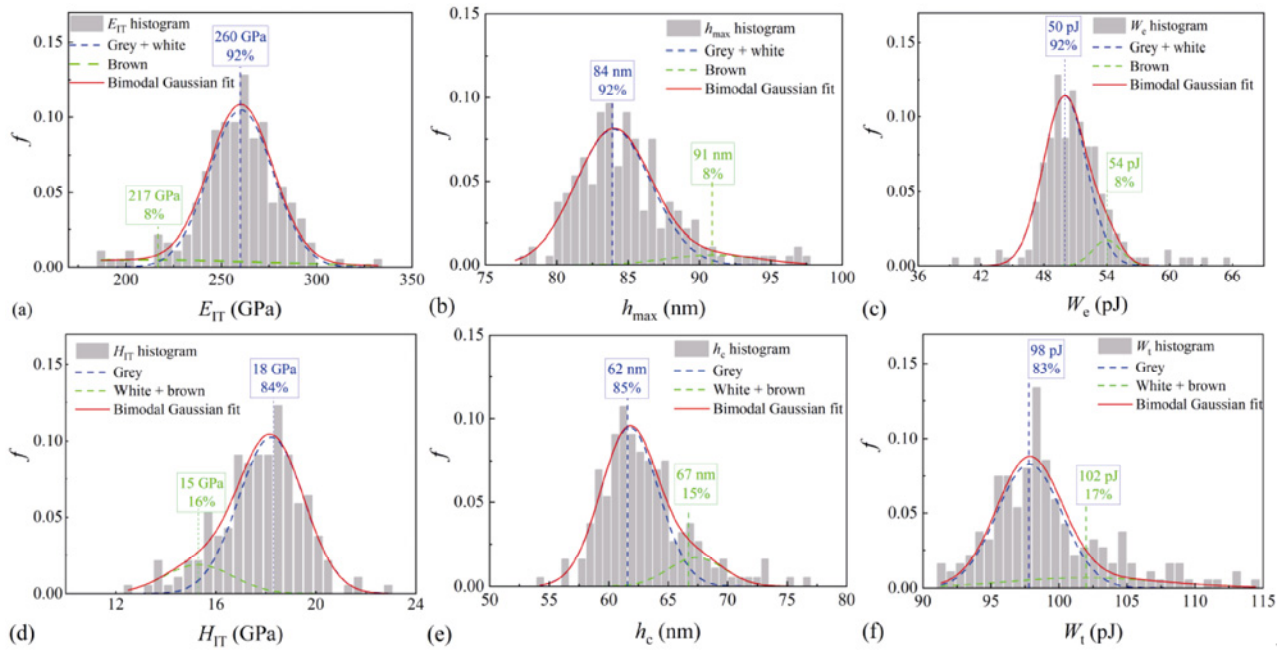
Fig. 3 Bimodal Gaussian distribution fittings (the nanoindentation results under F_{max} = 3 mN (Table 2) were used as the initial guess values of μ for the nonlinear curve fitting) of normalized probability density plots of indentation parameters of BST ceramic: (a) E_{IT}, (b) h_{max}, (c) W_e, (d) H_{IT}, (e) h_c, and (f) W_t.

Table 3 Volume fractions (%) of different regions of BST ceramic obtained by bimodal Gaussian fitting of nanoindentation parameters

Region	E_{IT}	h_{max}	W_e	H_{IT}	h_c	W_t
Grey substrate	92	92	92	84	85	83
White region				16	15	17
Brown region	8	8	8			

3. 3 Nanoindentation responses under various indentation loads

Figures 4(a) and 4(b) show the indentation load–displacement curves of BST ceramic under large and small loads, respectively: All loading portions follow the same trace; the unloading curves are nonlinear, and power-law fitting should be used; plastic deformation can be seen even under load as small as 1 mN; and creep is negligible for BST ceramic of little time-dependent deformation capability (i.e., creep [39] and inelasticity [101]). The surface cracks observed at the largest indentation load of 500 mN are too small to be measured (the inset of Fig. 4(a)), and the slight cracking indicates indentation-induced damage, resulting in deterioration of measured elastic modulus and hardness, based on which fracture toughness can be calculated by energy-based approaches without requiring measurement of crack length in Section 3.6.1.

Pop-ins, which are normally associated with severe surface damage, cannot be detected on load–displacement curves under the slight Berkovich indenter-induced surface cracking, based on which fracture toughness cannot be calculated, since the crack lengths are too small to be accurately measured. The W_e can be calculated as the area under the unloading curve; the W_t can be obtained by integrating the loading and holding segments of load–displacement curve [39,58]; the plastic deformation work ($W_p = W_t - W_e$) can be calculated as the net area enclosed by the loading and unloading curves [64,101]. Figures 4(c) and 4(d) show the variations of $h_p/F_{max}^{0.5}$ and $W_p/F_{max}^{1.5}$ with the maximum load F_{max}, respectively: Both $h_p/F_{max}^{0.5}$ and $W_p/F_{max}^{1.5}$ increase with F_{max} under small loads ($F_{max} < 25$ mN), which is ascribed to the elastic–plastic deformation of BST ceramic; the increasing rate becomes progressively smaller when the indentation load increases beyond a critical load $F_{max} = 25$ mN, which is the critical load for the initiation of fracture in Fig. 14(f); and constant values of $h_p/F_{max}^{0.5}$ and $W_p/F_{max}^{1.5}$ can be approximated under large loads, implying that steady-state damage accumulation is associated with constant levels of $h_p/F_{max}^{0.5}$ and $W_p/F_{max}^{1.5}$.
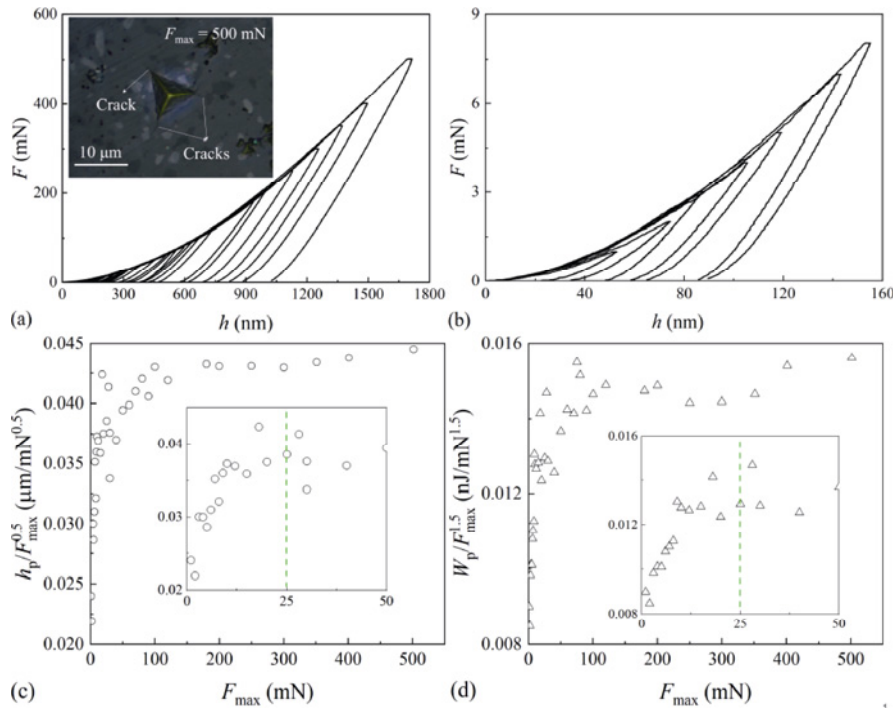
Fig. 4 Indentation load–displacement curves of BST under (a) large loads (the inset shows the cracks emanating from the corners of indentation imprint at F_{max} = 500 mN) and (b) small loads; variations of (c) $h_p/F_{max}^{0.5}$ and (d) $W_p/F_{max}^{1.5}$ with F_{max}.

Figure 5(a) shows that the m can be assumed to be a constant of 1.36, which lies in the normal range from 1.2 to 1.7 [39,64], and is almost the same as that of soda-lime glass (i.e., 1.37) [102]; the h_p is proportional to the h_{max}. The constant value of m is independent of load, and the proportional relationship between h_p and h_{max} has been widely reported in Refs. [37,58,64,103]. h_p/h_{max} is about 0.62 for BST ceramic and smaller than 0.7, indicating that there exists no pile-up [104], which is rational for brittle ceramics. With Eq. (1), S can be expressed as

$$S = \kappa \frac{F_{max}}{h_{max}}, \quad \kappa = m \frac{h_{max}}{h_{max} - h_p} = \frac{m}{1 - h_p/h_{max}} \quad (5)$$

where h_p/h_{max}, m, and κ can all be approximated to be

constant and independent of load, resulting in the proportional relationship between S and F_{max}/h_{max}. Therefore, S can be obtained from the loading without requiring unloading segment of the load–displacement curve. With m = 1.36 and h_p/h_{max} = 0.62, as shown in Fig. 5(a), κ can be calculated to be 3.6 by Eq. (5).

Gong *et al.* [59,63] have recently proposed a normalized equation for fitting the unloading segment, and S can be obtained from F_{max} and h_{max}.

$$\frac{F}{F_{max}} = \alpha_0 + \alpha_1 \left(\frac{h}{h_{max}} \right) + \alpha_2 \left(\frac{h}{h_{max}} \right)^2,$$
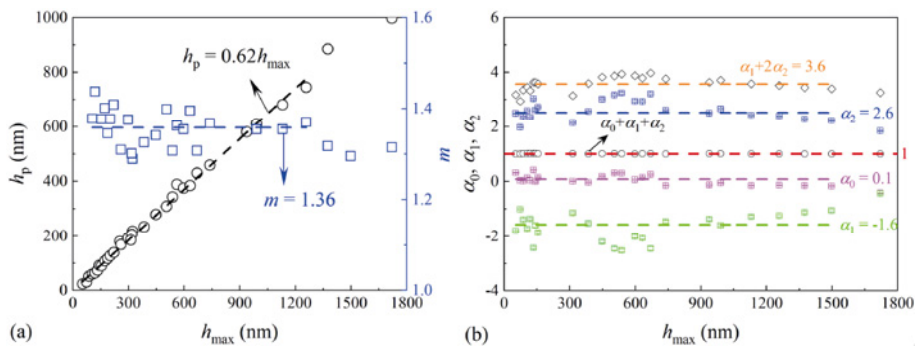$$S = \left(\frac{dF}{dh} \right)_{h=h_{max}} = \frac{F_{max}}{h_{max}} (\alpha_1 + 2\alpha_2) \quad (6)$$

Fig. 5 Variations of fitting parameters with h_{max}: (a) h_p and m of Eq. (1) and (b) α_0, α_1, and α_2 of Eq. (6).

where α_0, α_1, and α_2 are the fitting parameters. If the parameters α_1 and α_2 are constant and independent of F_{max}, the S can thus be determined continuously by using the loading segment rather than the unloading segment, resulting in the continuous measurement of S and h_c during loading, which is a revolutionary for the instrumented indentation technique, since both the elastic modulus and indentation hardness can be continuously obtained during loading without the need of unloading. The unloading segment of load–displacement data can be analyzed by Eq. (6), whose fitting parameters α_0, α_1, and α_2 are shown in Fig. 5(b). The sum of α_0, α_1, and α_2, which should equal to 1, is also included. All three fitting parameters can be approximated to be constant (i.e., $\alpha_0 = 0.1$, $\alpha_1 = -1.6$, and $\alpha_2 = 2.6$) and independent of load. Reference [63] showed that $\alpha_0 = -0.8$, $\alpha_1 = -0.2$, and $\alpha_2 = 2$ for soda-lime glass. The sum of α_1 and $2\alpha_2$ can be regarded to be a constant of 3.6 that is the same as κ by Eq. (5), indicating that S can be obtained from the loading segment of the load–displacement curve by Eq. (6). Figure 6(a) shows that the S calculated by Eq. (1) is proportional to that calculated by Gong theory Eq. (6) with the proportional coefficient of 0.94 being close to 1.

S relates to h_c by Eq. (7) [59]:

$$S^2 = c_0 + c_1 h_c + c_2 h_c^2 \tag{7}$$

where c_0, c_1, and c_2 are the fitting parameters. With a constant value of $\alpha_1 + 2\alpha_2 = 3.6$, as shown in Fig. 5(b), S can be obtained by Gong theory Eq. (6).

Comparing Eqs. (2) and (7), it is found that

$$S = \sqrt{\frac{4\beta^2 E_r^2}{\pi}}(A_p)^{1/2}$$
$$= \sqrt{\frac{c_2}{24.5}}\left(24.5 h_c^2 + \frac{24.5 c_1}{c_2} h_c + \frac{24.5 c_0}{c_2}\right)^{1/2} \tag{8}$$

where $24.5 h_c^2$ is the projected contact area of an ideal Berkovich indenter, and it can be deduced that [59]:

$$A_p(h_c) = 24.5 h_c^2 + \frac{24.5 c_1}{c_2} h_c + \frac{24.5 c_0}{c_2},$$
$$E_r = \frac{1}{2\beta}\sqrt{\frac{\pi c_2}{24.5}} \tag{9}$$

Figures 6(b) and 6(c) show the curve fittings of the variation of S^2 obtained by OP method Eq. (1) and Gong theory Eq. (6), with h_c by Eq. (7) under small ($h_c < 300$ nm) and large ($h_c > 300$ nm) h_c, respectively. Under small h_c, S^2 nonlinearly increases with h_c; and the constant term in Eq. (7) can be assumed to be zero (i.e., $c_0 = 0$). Under large h_c, S^2 increases with h_c
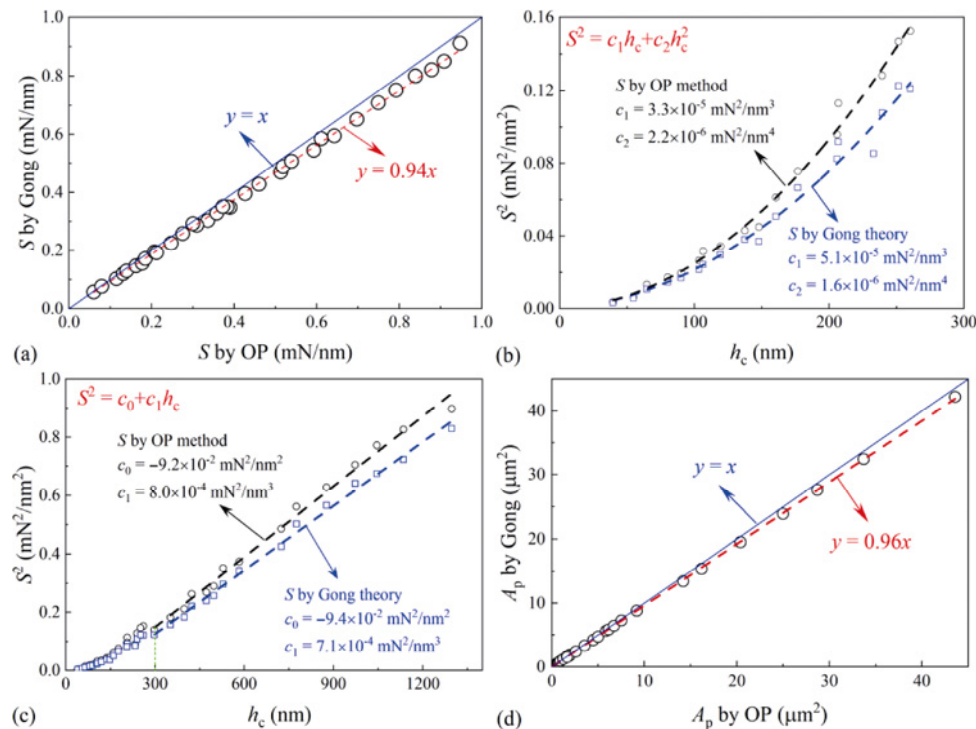

Fig. 6 Analysis of S: (a) comparison of S between Gong theory Eq. (6) and OP method Eq. (1); (b) variation of S^2 under small h_c; (c) variation of S^2 under large h_c; and (d) comparison of A_p between Gong theory Eq. (9) and OP method with B-spline interpolation.

in an approximately linear way; the quadratic term in Eq. (7) can be neglected (i.e., $c_2 = 0$). With $c_1 = 5.1 \times 10^{-5}$ mN^2/nm^3 and $c_2 = 1.6 \times 10^{-6}$ mN^2/nm^4 ($c_0 = 0$) obtained by Eq. (7) (Fig. 6(b)), the A_p under shallow indentation can be calculated by Gong theory Eq. (9). Figure 6(d) shows that the A_p calculated by OP method with B-spline interpolation is proportional to the A_p calculated by Gong theory Eq. (9) with the proportional coefficient of 0.96 being close to 1.

By substituting Eq. (9) into Eq. (2) with $c_0 = 0$, H_{IT} can be derived based on c_2 method for the first time:

$$H_{IT} = \frac{F_{max}}{24.5(h_c^2 + c_1/c_2\, h_c)} \quad (10)$$

where $c_1 = 5.1 \times 10^{-5}$ mN^2/nm^3, and $c_2 = 1.6 \times 10^{-6}$ mN^2/nm^4 by Gong theory for indentation of BST ceramic (Fig. 6(b)).

Cheng *et al.* [60–62] proposed a proportional relationship between the ratio of H_{IT} over E_r and the ratio of W_e over the W_t for conical indenters.

$$\frac{H_{IT}}{E_r} = \chi\frac{W_e}{W_t} = \frac{1}{\lambda(1+\gamma)}\frac{W_e}{W_t},$$
$$\lambda = 1.5\tan\theta + 0.327,\ \ 60° \leqslant \theta \leqslant 80° \quad (11)$$

where the proportionality factor (χ) is dependent on indenter geometry; and γ is a constant under large h_p/h_{max} (or W_p/W_t) [60].

$$\gamma = 0.27 \text{ for } \frac{h_p}{h_{max}} > 0.4 \text{ or } \frac{W_p}{W_t} = 1 - \frac{W_e}{W_t} > 0.2 \quad (12)$$

Since $h_p/h_{max} = 0.62 > 0.4$ (Fig. 5(a)), and $W_p/W_t = 1 - W_e/W_t = 0.54 > 0.2$ (Fig. 7(a)), with $\gamma = 0.27$ and $\lambda = 4.52$ for equivalent cone angle (θ) = 70.3° of Berkovich indenter, χ can be calculated to be 0.174, and lies within the reasonable range (i.e., 0.17–0.22) [64].

Equation (2) gives

$$\frac{H_{IT}}{E_r^2} = \frac{4\beta^2 F_{max}}{\pi S^2} \quad (13)$$

E_r and H_{IT} can be solved from Eqs. (11) and (13):

$$E_r = \frac{\pi S^2}{4\beta^2 F_{max}}\left(\chi\frac{W_e}{W_t}\right),\ H_{IT} = \frac{\pi S^2}{4\beta^2 F_{max}}\left(\chi\frac{W_e}{W_t}\right)^2 \quad (14)$$

where the ratio of F_{max} over S^2 can be regarded to be constant, and it is found $F_{max}/S^2 = 362$ nm^2/mN by curve fitting, as shown in Fig. 7(b).

With the proportional relationship between S and the ratio of F_{max} over h_{max} proposed by Gong theory Eq. (6), Eq. (14) can be transformed to

$$E_r = \frac{\pi F_{max}}{4\beta^2 h_{max}^2}(\alpha_1 + 2\alpha_2)^2\left(\chi\frac{W_e}{W_t}\right),$$
$$H_{IT} = \frac{\pi F_{max}}{4\beta^2 h_{max}^2}(\alpha_1 + 2\alpha_2)^2\left(\chi\frac{W_e}{W_t}\right)^2 \quad (15)$$

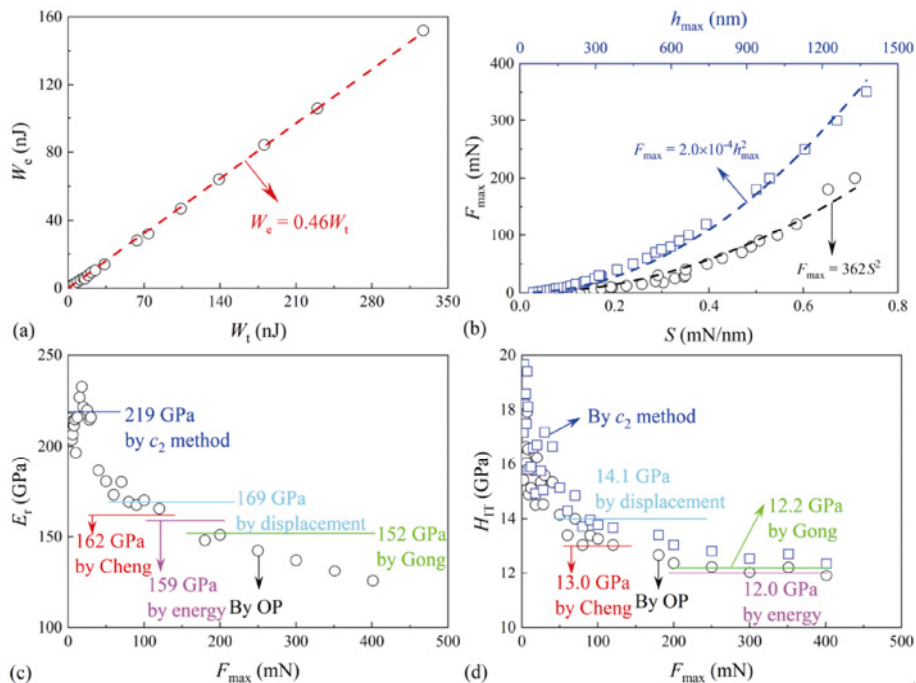**Fig. 7** Analysis of E_r and H_{IT} obtained by different methodologies: (a) proportional relationship between W_e and W_t; (b) quadratic dependence of F_{max} on h_{max} and S; and (c) E_r and (d) H_{IT} obtained by different methods.

where $\alpha_1 + 2\alpha_2 = 3.6$ (Fig. 5(b)), F_{max} can be regarded to be proportional to the square of h_{max} [105], and it is found that $F_{max}/h_{max}^2 = 2.0 \times 10^{-4}$ mN/nm² (Fig. 7(b)).

An alternative energy-based approach of calculating H_{IT} and E_r was proposed without the need of $A_p(h_c)$ [64].

$$E_r = \left[\frac{2\cot\theta W_e/W_t}{3\pi m/(m+1)-\pi\varepsilon W_e/W_t}\right]\bigg/\left(\frac{4\beta F_{max}}{\pi S^2}\right),$$

$$H_{IT} = \left[\frac{2\cot\theta W_e/W_t}{3\pi m/(m+1)-\pi\varepsilon W_e/W_t}\right]^2\bigg/\left(\frac{4\beta F_{max}}{\pi S^2}\right) \quad (16)$$

where $\theta = 70.3°$, $\beta = 1.034$, and $\varepsilon = 0.75$ for Berkovich indenter.

With constant values of $m = 1.36$ and $h_p/h_{max} = 0.62$, a permanent displacement-based approach was developed as [64]:

$$E_r = \frac{(1-h_p/h_{max})S^2\cot\theta}{2\beta F_{max}[m-\varepsilon(1-h_p/h_{max})]},$$

$$H_{IT} = \frac{(1-h_p/h_{max})^2 S^2\cot^2\theta}{\pi F_{max}[m-\varepsilon(1-h_p/h_{max})]^2} \quad (17)$$

Figure 7(c) compares the values of E_r by various equations: $E_r = 162$ GPa by Cheng theory (Eq. (14)), $E_r = 152$ GPa by Gong theory (Eq. (15)), $E_r = 159$ GPa by energy-based approach (Eq. (16)), $E_r = 169$ GPa by displacement-based approach (Eq. (17)), and $E_r = 219$ GPa by c_2 method (Eq. (9)) with $c_2 = 1.6 \times 10^{-6}$ mN²/nm⁴ obtained under small h_c (< 300 nm) or F_{max} (< 40 mN) (Fig. 6(b)). E_r obtained by OP method (Eq. (2)) lies within the range from 120 to 230 GPa and decreases with F_{max} due to the accumulation of indentation-induced damage in the brittle ceramics. E_r obtained by OP method (Eq. (2)) varies with F_{max}, while the values of E_r obtained by other methods, which do not require area function of the indenter, are based on the scaling relationships among indention parameters (i.e., h_p/h_{max}, W_e/W_t, F_{max}/h_{max}^2, and F_{max}/S^2), which are obtained based on all the nanoindentation data under various loads, resulting in a single value of E_r for each method. $E_r = 169$ GPa by displacement-based approach (Eq. (17)) is a little larger than $E_r = 162$ GPa by Cheng theory (Eq. (14)). E_r by Cheng theory is close to $E_r = 159$ GPa by energy-based approach (Eq. (16)). E_r by energy-based approach is a little larger than $E_r = 152$ GPa by Gong theory (Eq. (15)). The plane strain modulus ($E^* = E/(1-v^2)$) was measured to be 232 GPa by resonant ultrasound spectroscopy, and E^* measured

on local region of little defect by nanoindentation is expected to be larger than that measured by resonant ultrasound spectroscopy, since the defect of bulk ceramics used in resonant ultrasound spectroscopy can deteriorate the elastic modulus of the brittle BST ceramic. It is found that only E^* (i.e., 271 GPa) obtained by c_2 method (Eq. (9)) under small loads is larger than that measured by resonant ultrasound spectroscopy, and the values of E^* measured by other methods (e.g., displacement-based approach, energy-based approach, Cheng theory, and Gong theory) are far less than that by c_2 method (Eq. (9)). Moreover, a constant level of E_r (i.e., 216 GPa) by OP method, as shown in Fig. 14(f), can be approximated under small loads with little indentation-induced damage and is consistent with that by c_2 method (Eq. (9)). It is worth noting that $c_2 = 1.6 \times 10^{-6}$ mN²/nm⁴ used in c_2 method is obtained under small loads, under which condition effect of indentation-induced damage can be neglected, while other methods (e.g., displacement-based approach, energy-based approach, Cheng theory, and Gong theory) are based on all the nanoindentation data under loads ranging from 0.1 to 500 mN, and the results can be affected by the nanoindentation data under large loads, which should not be used due to the significant effect of indention-induced damage on mechanical performance of brittle ceramics. Therefore, c_2 method (Eq. (9)) is believed to be the most suitable to characterize the elastic modulus of brittle ceramics, and the measurement of both elastic modulus and indentation hardness by nanoindentation should be performed under small loads in order to avoid indentation-induced damage.

Figure 7(d) compares the values of H_{IT} obtained by various methods: $H_{IT} = 13.0$ GPa by Cheng theory (Eq. (14)), $H_{IT} = 12.2$ GPa by Gong theory (Eq. (15)), $H_{IT} = 12.0$ GPa by energy-based approach (Eq. (16)), and $H_{IT} = 14.1$ GPa by displacement-based approach (Eq. (17)). The values of H_{IT} by OP method (Eq. (2)) and by c_2 method (Eq. (10)) are almost the same with each other. The values of H_{IT} obtained by c_2 method (Eq. (10)) and OP method vary with the F_{max}, while only a single value of H_{IT} can be obtained by other methods, which rely on the scaling indentation relationships obtained by all nanoindentation data under various loads. H_{IT} decreases from 19 to 12 GPa with the increase in F_{max} due to indentation-induced damage, which is also corroborated by the decrease in E_r. $H_{IT} = 14.1$ GPa by displacement-based approach (Eq. (17)) is a little larger than $H_{IT} = 13.0$ GPa by

Cheng theory (Eq. (14)), which is a little larger than H_{IT} = 12.2 GPa calculated by Gong theory (Eq. (15)), which is almost the same as H_{IT} = 12.0 GPa by energy-based approach (Eq. (16)). H_{IT} measured under very small loads is unreliable and subject to many factors such as indentation size effect [106,107], surface effects, work hardening [108], and the blunt tip of the indenter; H_{IT} measured under relatively large indentation loads is influenced by indentation-induced damage. H_{IT} would be underestimated when all the nanoindentation data were used for calculation, and accurate determination of indentation hardness of brittle BST ceramic by OP method (Eq. (2)) also requires small loads, under which condition a constant level of H_{IT} can be approximated without the influence of indentation-induced damage, and it is found that H_{IT} = 16.2 GPa, as shown in Fig. 14(f).

3. 4 Elastic modulus obtained by H_K

The macroscopic elastic modulus (E_K) can also be obtained based on the elastic recovery of imprint by Knoop indenter [65].

$$\frac{b}{d} = \frac{1}{7.11} - \frac{\alpha_K H_K}{E_K}, \quad H_K = \frac{2P \tan \theta_1}{d^2 \tan \theta_2} = \frac{14.229P}{d^2} \quad (18)$$

where d and b are the long and short diagonals of residual imprint, respectively; α_K is a constant of 0.45 for ceramics [109]; H_K is the Knoop hardness, which is the mean pressure defined by the ratio of normal load (P) over the projected area of residual imprint created by the lozenge-based pyramid Knoop indenter [110]; and θ_1 (= 86.25°) and θ_2 (= 65°) are the semi-apical angles of Knoop indenter.

Figure 8(a) shows the residual imprint by Knoop indenter at the load of 1000 gf, and no cracking on the surface is observed due to the flatness and bluntness of Knoop indenter resulting from its specific elongated rhombohedral shape, which results in much less damage than those of Berkovich and Vickers indenters under the same normal load [110,111]. Knoop indenter is more appropriate for investigating microhardness of brittle solids, and thus, a much larger load is required for the calculation of fracture toughness of BST ceramic by Knoop indenter-induced cracking method [112]. With a constant b/d of 0.126 by linear fitting (Fig. 8(b)) and α_K = 0.45, E_K can be calculated by Eq. (18) with known H_K. Figure 8(c) shows that both H_K and E_K decrease with P and reach constant levels under large P. E_K under large loads of 4.9 and 9.8 N are almost the same as the average value (i.e., E_{IT} = 260 GPa
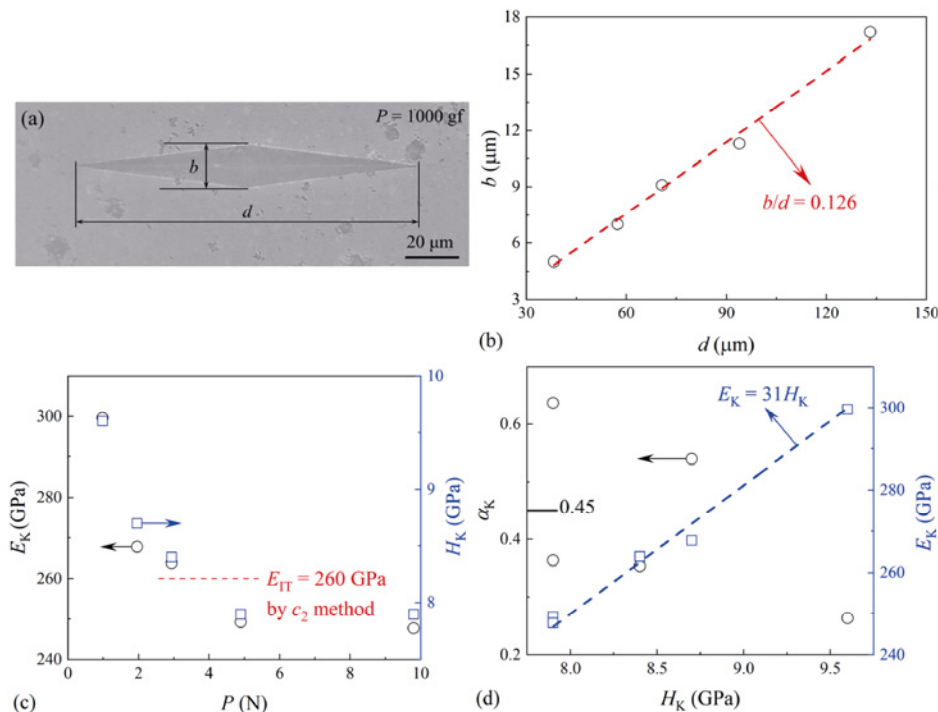

Fig. 8 Analysis of E_K based on H_K technique under various loads and dwell time of 15 s on a microhardness tester (MHVKN-1000, Shanghai Jvjing Precision Instrument Manufacturing Co., Ltd., Shanghai, China): (a) residual imprint by Knoop indenter under P = 1000 gf; (b) proportional relationship between b and d; (c) variations of E_K and H_K with P; and (d) dependence of α_K and E_K on H_K.

that can be obtained from E_r) of elastic modulus by c_2 method, demonstrating the applicability of H_K to estimation of elastic modulus of dielectric ceramics. It is interesting to note that E_K is proportional to H_K, which was also reported for bulk metallic glasses [113], and $E_K = 31H_K$ for BST ceramic (Fig. 8(d)).

With a constant E_{IT} obtained by nanoindentation, α_K can be calculated from Eq. (18) as

$$\alpha_K = \frac{E_{IT}}{H_K}\left(\frac{1}{7.11} - \frac{b}{d}\right) \quad (19)$$

where $b/d = 0.126$ (Fig. 8(b)) and $E_{IT} = 260$ GPa calculated by substituting $E_r = 219$ obtained by c_2 method Eq. (9) into Eq. (2). Figure 8(d) shows that the values of α_K obtained by Eq. (19) are more or less than the constant of 0.45 proposed for ceramics [109], indicating the validity of $\alpha_K = 0.45$ for BST ceramic.

3. 5 Microscratch responses of BST ceramic

Figures 9(a) and 9(b) show the variations of scratch variables such as penetration depth (d_p), residual depth

(d_r) representing plastic deformation, horizontal force (F_h), friction coefficient ($\mu_s = F_h/F_n$), and AE, with applied F_n during scratching by Berkovich and spherical indenters. Chips and cracking at some weaker points of brittle BST ceramic are induced by Berkovich indenter due to the sharp edge of Berkovich indenter, as expected in Ref. [114]. Scratch groove and surface cracking are invisible by spherical indenter due to the bluntness of spherical indenter. For a spherical indenter, d_p increases proportionally with F_n, which is consistent with the result of copper [71]; the negligible d_r obtained by spherical indenter indicates that elastic deformation plays the predominant role during scratch by a spherical indenter due to its blunt tip; and AE remains a low and constant level without fluctuation in the absence of surface cracking. The significantly smaller μ_s under a spherical indenter than μ_s under Berkovich indenter is due to the much shallower penetration depth and the smooth shape of the spherical indenter.
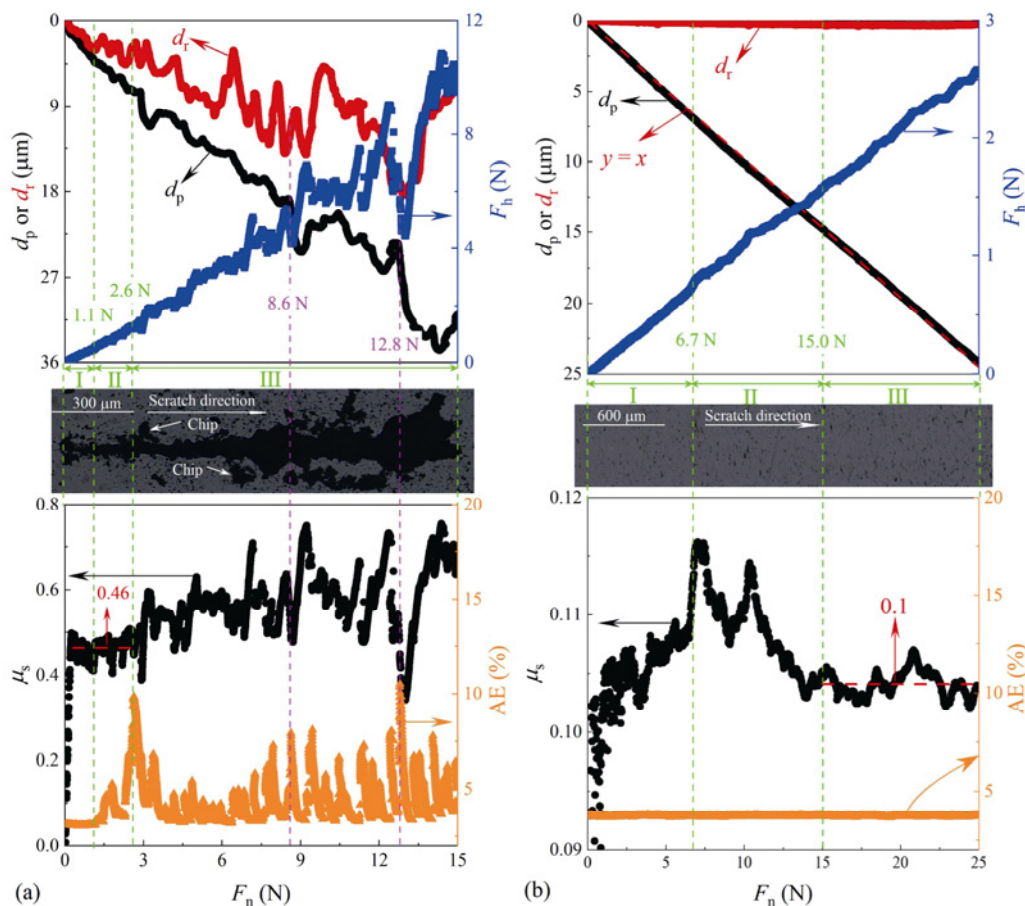
For Berkovich indenter (Fig. 9(a)), three different

Fig. 9 Variations of d_p, d_r, F_h, μ_s, and AE with applied F_n during scratching by (a) Berkovich indenter and (b) spherical indenter. The optical images of residual scratch grooves by Berkovich and spherical indenters are synchronized with scratch variables.

regimes with two demarcation points can be identified. The first demarcation point (F_n = 1.1 N) distinguishing regime I and regime II can be identified by the sudden increase in AE and the beginning of fluctuation of d_r. During regime I for low loads (F_n < 1.1 N), AE remains a low and constant level without fluctuation; d_p, d_r, F_h, and F_n all have proportional relationships. AE fluctuates during regime II when severe surface cracking appears. The second demarcation point (F_n = 2.6 N) distinguishing regime II and regime III can be identified by the sudden increase in both d_p and μ_s. Both d_r and AE fluctuate during regime II for intermediate loads (1.1 N < F_n < 2.6 N). A constant μ_s (about 0.46) can be approximated (i.e., F_h is proportional to F_n) during regimes I and II with the slight data fluctuation due to scratch-induced vibration of the sample surface [115,116]. All variables including d_p, d_r, F_h, and μ_s fluctuate dramatically during regime III for high loads (F_n > 2.6 N) due to the severe cracking and damage [117]. The abrupt increase in AE correlates closely with the abrupt decrease in both F_h and μ_s and is also associated with a rapid increase in d_p (F_n = 8.6 and 12.8 N highlighted in Fig. 9(a) for two examples).

For a spherical indenter (Fig. 9(b)), three different regimes with two demarcation points can also be identified. The first demarcation point (F_n = 6.7 N) distinguishing regime I and regime II can be identified by the sudden increase in both μ_s and F_h. During regime I for low loads (F_n < 6.7 N), a constant μ_s can be approximated when the adhesion plays the predominant role [118], and F_h is proportional to F_n in the absence of data fluctuation. During regime II for intermediate loads (6.7 N < F_n < 15.0 N), μ_s fluctuates due to fluctuation of F_h and tends to decrease due to cracking/damage beneath the surface. A constant μ_s (about 0.1, F_h is proportional to F_n) can be approximated during regime III for high loads (F_n > 15.0 N), indicating the stable propagation of cracking in the subsurface region, which meets the assumption of a semi-circular cracking plane beneath the surface used for calculation of fracture toughness by the scratch approach (Fig. 10). The second demarcation point (F_n = 15.0 N) distinguishing regime II and regime III can be identified by the intersection between the constant level of μ_s during regime III and the varying trend during regime II. Although little surface damage can be observed by a spherical indenter, subsurface damage is indicated by the sudden change of μ_s, and

LEFM is expected to be applicable to assessment of fracture toughness.

The S_h, S_n, and l_p between Berkovich (or spherical) indenter and the sample can be calculated from d_p according to the geometrical intersection model, as shown in Fig. 10 and Eq. (20).

$$
\left. \begin{aligned}
l_p &= 2d_p\sqrt{3\tan^2\alpha_B + 1} \\
S_h &= \sqrt{3}d_p^2\tan\alpha_B \\
S_n &= 2\sqrt{3}d_p^2\tan^2\alpha_B
\end{aligned} \right\} \text{ for Berkovich indenter}
$$

$$
\left. \begin{aligned}
l_p &= 2R\arccos\frac{R-d_p}{R} \\
S_h &= R^2\arccos\frac{R-d_p}{R} - \\
&\quad (R-d_p)\sqrt{R^2-(R-d_p)^2} \\
S_n &= \frac{\pi}{2}(2R-d_p)d_p
\end{aligned} \right\} \text{ for spherical indenter}
$$

(20)

where α_B = 65.27° for Berkovich indenter, and tip radius (R) = 500 μm for the spherical indenter used in the current study.

The horizontal scratch hardness (H_h) and normal scratch hardness (H_n) can be calculated as the mean pressures defined by the ratio of F_h over the S_h and by the ratio of F_n over the S_n, respectively.

$$H_h = F_h/S_h, \quad H_n = F_n/S_n \tag{21}$$

Figures 11(a) and 11(b) show the variations of H_h and H_n with the applied F_n by Berkovich and spherical indenters, respectively, and power-law functions are applicable to describe their variations with F_n. Both H_h and H_n decrease with the increasing F_n for Berkovich indenter. For the spherical indenter, H_h decreases, while H_n increases with F_n, resulting a transition point (i.e., 15 N) for equality between H_h and H_n: H_h is larger than H_n under small F_n (< 15 N); H_h is small than H_n under large F_n (> 15 N). It is interesting to note that the transition point of 15 N is right the same as the secondary demarcation point, as shown in Fig. 9(b), and the transition point between regime II and regime III for a spherical indenter can be obtained by the equality between H_h and H_n. It is also interesting to note that the values of power-law exponents are the same (i.e., −0.4) for H_h and H_n by Berkovich indenter, resulting in the proportional relationship between H_h and H_n (i.e., H_h = 3.7H_n) by Berkovich indenter; and H_n for Berkovich indenter is almost the same as H_h for the spherical indenter with R = 500 μm. Figure 11(c)
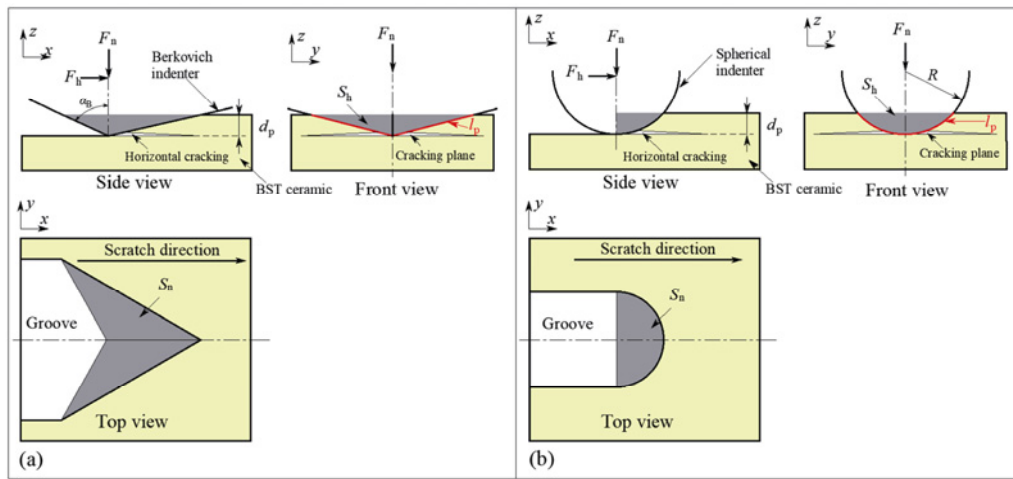
Fig. 10 Schematic illustrations of geometrical parameters during scratching with cracking assumption (i.e., a semi-circular horizontal crack emanates from indenter tip) for calculating fracture toughness: (a) Berkovich and (b) spherical indenters. Note: S_h, S_n, and l_p denote the horizontally projected contact area, normally projected contact area, and perimeter length, respectively, and α_B is the face angle of Berkovich indenter
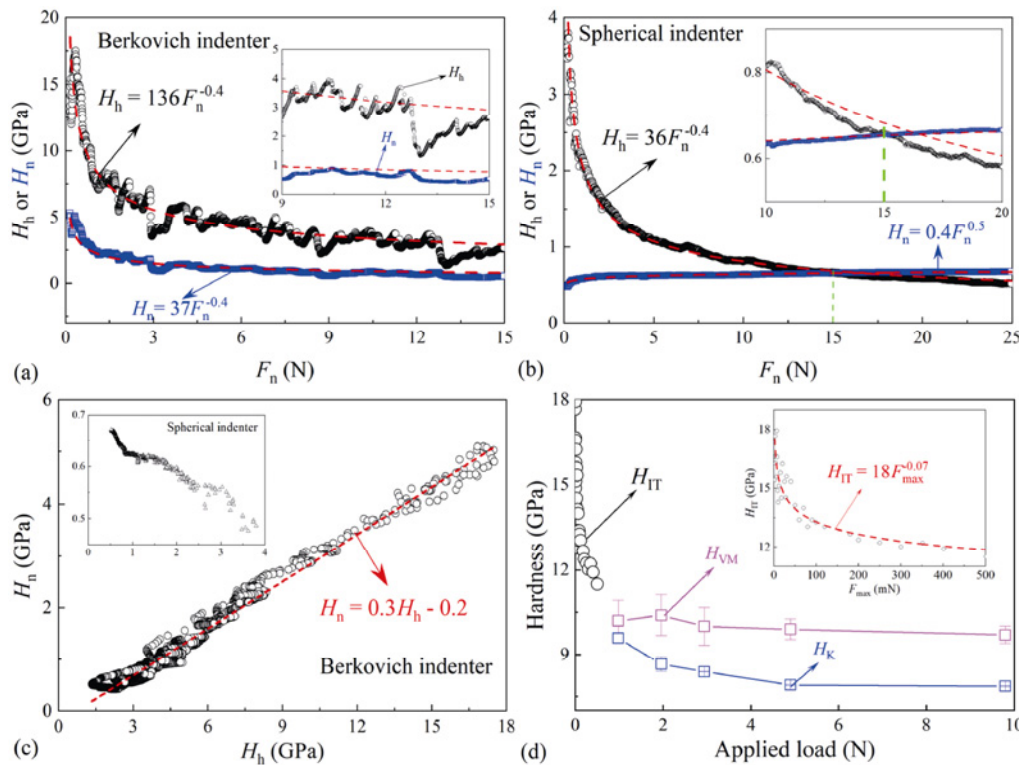

Fig. 11 Variations of various hardness values with load: (a) H_h and H_n by Berkovich indenter; (b) H_h and H_n by spherical indenter; (c) relationships between H_n and H_h for Berkovich and spherical indenters; and (d) comparison of hardness values obtained by different techniques (i.e., H_{IT} by Berkovich nanoindentation, H_{VM} by Vickers indenter, and H_K by Knoop indenter).

shows that a linear relationship between H_n and H_h can be approximated for Berkovich indenter, while a linear relationship between H_n and H_h can only be approximated under large loads for a spherical indenter. Figure 11(d) compares the hardness values obtained by different indenters: H_{IT} by Berkovich indenter decreases with F_{max} due to indentation-induced damage, and a

power-low function can be used to describe its variation with F_{max}; H_K by Knoop indenter (Eq. (18)) and H_{VM} by Vickers indenter (Eq. (22)) both decrease with the increase in the applied normal load, which can be explained by noting indentation size effect [106,107] and indentation-induced damage; the values of H_K by Knoop indenter are smaller than those of H_{VM} by

Vickers indenter, since Knoop impression exhibits a smaller elastic recovery than Vickers impression due to the longer diagonal of Knoop indenter, especially for nonmetals like ceramics and hard materials [109,119–122]. The larger fluctuation of H_{VM} than that of H_K is caused by surface cracking induced by Vickers indenter, as shown in Fig. 12(a). The values of hardness obtained by normal indentation (i.e., H_{IT}, H_K, and H_{VM}) are much larger than those obtained by scratch test, since scratching can induce more severe damage to the material.

3.6 Fracture toughness of brittle BST ceramic

3.6.1 Vickers indenter-induced cracking method

Microhardness tests were conducted with Vickers indenters on the microhardness tester (MHVKN-1000, Shanghai Jvjing Precision Instrument Manufacturing Co., Ltd., Shanghai, China) under dwell time of 15 s and five different loads (i.e., 100, 200, 300, 500, and 1000 gf) with 20 repetitive tests being carried out under each normal load level. H_{VM} can be calculated by the ratio of P over the projected area of residual imprint of Vickers indenter.

$$H_{VM} = \frac{P}{2a^2} \tag{22}$$

where a is the average length of the two diagonals of

residual imprint by Vickers indenter.

Figure 12(a) shows the residual imprint by Vickers indenter at P = 1000 gf. The indenter-induced cracking has become an effective technique to estimate fracture toughness of brittle ceramics for the past four decades [112,123–125]. Vickers indenter can induce two cracking modes (i.e., radial and median cracking modes) [24], as shown in Fig. 12(b): Radial cracking emanates from the four corners of diagonals of the imprint; and median cracking initiates beneath the imprint. The absence of multiple or chaotic cracking [126] indicates the good quality and homogeneity of the prepared BST ceramic, whose relative density is about 94%. The average values of a, c, l/a, and H_{VM} based on 20 repeated tests under each load are listed in Table 4. The cracking mode of BST ceramic is radial (or Palmqvist) cracking under the condition of $0.25 \leqslant l/a \leqslant 2.5$ [127–129]. Equations (23)–(35) for calculating K_C are listed in Table 5. The critical variables such as $P/c^{1.5}$ and $l^{-0.5}a$ for calculating K_C are also listed in Table 4. a, c, and l/a all increase with P, indicating that the damage and cracking with deformation become more severe with the increasing normal load; while H_{VM}, $P/c^{1.5}$, and $l^{-0.5}a$ can be regarded as constant values of 10 GPa, 24.5 mN/μm$^{1.5}$, and 3.7 μm$^{0.5}$, respectively. The values of K_C calculated by different equations are listed in Table 6.
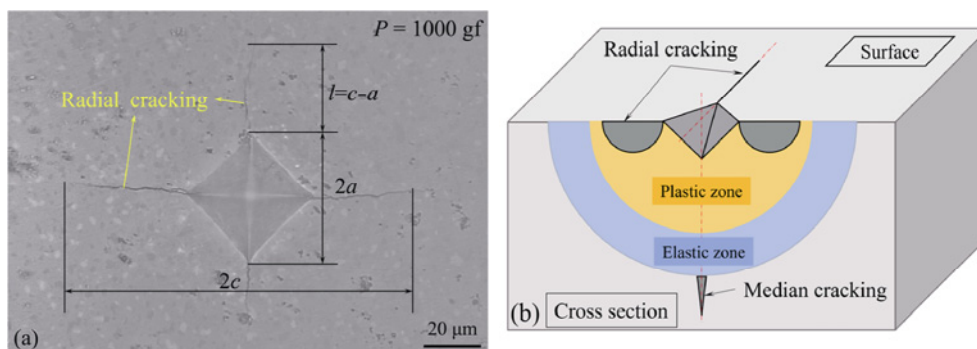

Fig. 12 Analysis of deformation and cracking by Vickers indenter: (a) residual imprint by Vickers indenter at P = 1000 gf ($2a$ is the diagonal of Vickers indent, l is half of the surface crack length for radial cracking, and $c = l + a$); (b) illustration of radial and median cracking modes.

Table 4 Average values of a, c, l/a, and H_{VM} under different P

P (gf)	a (μm)	c (μm)	l/a	H_{VM} (GPa)	$P/c^{1.5}$ (mN/μm$^{1.5}$)	$l^{-0.5}a$ (μm$^{0.5}$)
100	6.9	—	—	10.2	—	—
200	9.7	16.4	0.7	10.4	29.5	3.7
300	12.1	24.4	1.0	10.0	24.4	3.5
500	15.7	33.7	1.1	9.9	25.0	3.7
1000	22.5	55.1	1.4	9.7	24.0	3.9

Note: P should be converted from gf to mN in the calculation of H_{VM}, and cracking is absent under small P ($\leqslant$ 100 gf).

Table 5 Equations (23)–(35) for calculation of K_C by Vickers indenter-induced cracking

Cracking type	Material and Ref.	Equation
Radial	Si_3N_4, SiC, B_4C, and soda-lime silica glass [130] and WC–Co [129]	$0.035(l/a)^{-0.5}[H_{VM}/(\phi E)]^{-0.4}(H_{VM}a^{0.5}/\phi)$ (23)
	ZnS, Si, and soda-lime glass [131]	$0.036 \times 10^{1.8}E^{0.4}P^{0.6}(2a)^{-0.7}(l/a)^{-1.5}$ (24)
	Ceramics [132]	$0.015(l/a)^{-0.5}(E/H_{VM})^{2/3}(P/c^{1.5})$ (25)
	WC–Co [133]	$\beta_V(H_{VM}P/4l)^{0.5}$ (26)
Median	Si, quartz, fused silica, and soda-lime silica glass [134]	$(1-2v)[(2H_{VM}/\pi)(P/c)]^{0.5}/(2\sqrt{2}\pi^2)$ (27)
	Si and SiC [135]	$72.5(P/c^{1.5})$ (28)
	Soda-lime silica glass [136]	$72.6(P/c^{1.5})$ (29)
	WC–Co, Si_3N_4, SiC, BC, ZnS, ZnSe, sapphire, and spinel [137]	$75.2(P/c^{1.5})$ (30)
	Si_3N_4, Al_2O_3, C9606, and glass [138]	$16(E/H_{VM})^{0.5}(P/c^{1.5})$ (31)
	WC–Co [129]	$0.129(c/a)^{-1.5}[H_{VM}/(\phi E)]^{-0.4}(H_{VM}a^{0.5}/\phi)$ (32)
R–M	Si and SiC [139]	$10^y[H_{VM}/(\phi E)]^{-0.4}H_{VM}a^{0.5}$ (33)
	α-SiC, Al_2O_3, soda-lime glass, and NaCl [140]	$0.0473(c/a)^{-1.56}[H_{VM}/(\phi E)]^{-0.4}H_{VM}a^{0.5}$ (34)
	Al_2O_3 [141]	$0.0183\lg(8.4a/c)[H_{VM}/(\phi E)]^{-0.4}H_{VM}a^{0.5}$ (35)

Note: "R–M" represents the mixture of radial and median cracking modes; P is the normal load for Vickers indenter; ϕ (= 3) is the constraint factor; v of BST ceramic is assumed to be 0.2; $\beta_V = 1/[3\pi(1-v^2)(\sqrt{2}\tan\psi)^{0.5}] = 0.06$ with half angle ($\psi = 68°$) for Vickers indenter; and $y = -1.59 - 0.34x - 2.02x^2 + 11.23x^3 - 24.97x^4 + 16.32x^5$, $x = \lg(c/a)$.

Table 6 K_C (MPa·m$^{1/2}$) of BST ceramic calculated by Eqs. (23)–(35) in Table 5

P (gf)	Radial				Median						R–M		
	Eq. (23)	Eq. (24)	Eq. (25)	Eq. (26)	Eq. (27)	Eq. (28)	Eq. (29)	Eq. (30)	Eq. (31)	Eq. (32)	Eq. (33)	Eq. (34)	Eq. (35)
200	2.5	6.9	3.9	1.6	0.6	1.8	1.8	1.8	2.0	**3.5**	3.6	3.7	2.3
300	2.5	4.2	3.2	1.4	0.6	1.8	1.8	1.8	2.0	**3.0**	3.7	**3.1**	2.3
500	2.5	4.0	3.0	1.5	0.7	1.8	1.8	1.8	2.0	**3.1**	4.0	**3.3**	2.5
1000	2.5	3.3	2.7	1.6	0.7	1.8	1.8	1.8	2.0	**3.0**	4.4	**3.2**	2.7

Note: The constant values of $E = 260$ GPa determined by Eq. (9), $H_{VM} = 10$ GPa, $P/c^{1.5} = 24.5$ mN/μm$^{1.5}$, and $\Gamma^{-0.5}a = 3.7$ μm$^{0.5}$ are used; the average values of c and a listed in Table 4 are used.

Values of K_C calculated by Eqs. (24), (25), (33), and (35) are load-dependent, and those equations cannot be applied to characterize fracture toughness of ceramics. Values of K_C calculated by Eqs. (23) and (26)–(31) can be approximated to be constant and independent of load. Values of K_C calculated by Eqs. (28)–(30) are almost the same, since those equations are almost the same with only a slight difference in the prefactor. Values of K_C calculated by Eqs. (32) and (34) can be approximated to be constant under large P with the relatively large values of K_C calculated under small P (< 300 gf) owing to the large measurement uncertainty of imprint diagonal and crack lengths.

Values of K_C calculated by Eqs. (32) and (34) under large P (> 200 gf) are about 3.1 and 3.2 MPa·m$^{1/2}$, respectively, and lie within the reasonable range (i.e., 3–4 MPa·m$^{1/2}$ by the single-edge notch beam method [142–145]) of dense dielectric ceramics. Based on the results of K_C by Eqs. (32) and (34) under large P (> 200 gf), K_C of BST ceramic is about 3.1 MPa·m$^{1/2}$. The

close values of K_C calculated by Eqs. (32) and (34) are due to their similar expressions. Nevertheless, Eq. (32) is more preferable than Eq. (34), since the power exponent of the term c/a is −1.5 in Eq. (32) rather than −1.56 in Eq. (34). Therefore, Eq. (32) is the most suitable expression for calculating fracture toughness of brittle BST ceramic based on Vickers indenter-induced cracking under relatively large loads. Although values of K_C calculated by Eqs. (23) and (26)–(31) are smaller than the reasonable value (i.e., 3.1 MPa·m$^{1/2}$), the empirical constants of those equations can be simply modified to give reasonable values of K_C: The prefactor 0.035 in Eq. (23) should be changed to 0.043; the prefactor 0.06 in Eq. (26) should be changed to 0.074; the prefactor in Eqs. (28)–(30) should be 93.6; and the prefactor in Eq. (31) should be 20 rather than 16.

The probability density function for cracking length follows Weibull [146] or Gaussian distribution [7]. Since Weibull distribution has been widely used to assess the statistical variation of strength [147] or the

measured cracking length of brittle materials (e.g., ceramics [148,149] and glasses [150]), and values of fracture toughness obtained by 40 measurements of $2c$ under each load were analyzed by the well-known two-parameter Weibull distribution equation [149,151]:

$$\ln\ln\left(\frac{1}{1-P_w}\right) = m\ln K_C - m\ln K_{C_0},$$
$$P_w = (i-0.5)/N \qquad (36)$$

where P_w is the cumulative probability of occurrence of $(K_C)_i$, which is the i-th ($1 \leqslant i \leqslant N$, N is the total number of data) result by ordering values of K_C from the lowest to the highest; m is the dimensionless Weibull modulus; and K_{C_0} is the scale parameter, which has the same unit as K_C. Figures 13(a) and 13(b) show the cumulative probability of normalized fracture toughness (i.e., K_C/K_{ca}, K_{ca} is the arithmetic average value of K_C by Eq. (23) from 40 measurements) and Weibull plots of K_C, respectively, for the datasets obtained at loads of 200, 300, 500, and 1000 gf. Although the difference among different loads seems slight (Fig. 13(a)), the results under different loads can be clearly differentiated (Fig. 13(b)). There exists a bilinear relationship between $\ln\ln(1/(1-P_w))$ and $\ln K_C$ for load of 200 gf, which can be explained by noting the large measurement uncertainty of small crack lengths under a small load; linear relationships between $\ln\ln(1/(1-P_w))$ and $\ln K_C$ are observed for loads of 300, 500, and 1000 gf, implying that the experimental data can be well described by the two-parameter Weibull equation.

The resultant Weibull parameters (i.e., m and K_{C_0}) for each dataset of K_C measured at different loads are summarized in Table 7. The minimum value (K_{min}), the maximum value (K_{max}), K_{ca}, and SD of the calculated values of K_C by Eq. (23) are also listed in Table 7. SD

is larger under the load of 200 gf due to the large measurement uncertainty of small crack lengths. The values of SD are the same for the three other loads (i.e., 300, 500, and 1000 gf), indicating that crack lengths can be accurately measured under loads no less than 300 gf. The difference between K_{max} and K_{min} becomes smaller as the load increases, indicating that a more reliable K_C can be measured under a larger load. m and K_{C_0} were obtained under small K_C (< 2.7 MPa·m$^{1/2}$, i.e., the first linear segment) for 200 gf, since only the first linear segment of its bilinear relationship between $\ln\ln(1/(1-P_w))$ and $\ln K_C$ is consistent with the results for larger loads.

The values of m and K_{C_0} are the same for loads of 200 and 500 gf, since the first linear segment for 200 gf almost coincides with the data for 500 gf. K_{ca}, which is the arithmetic average of K_C from 20 repeated tests under each load level, is almost the same as K_{C_0}, implying that 20 repeated tests are sufficient to obtain a reasonable value of fracture toughness of BST ceramic. m, which is normally larger than 100 for metals [152], indicates the quality and brittleness of ceramics. m of BST ceramic lies within the reasonable range of 10–20, since m of ceramics is normally smaller than 20 [153] (e.g., $m = 15$ for Si$_3$N$_4$ [154], $m = 19.8$ for ZrO$_2$ [154], and $m = 16$ for porcelain [155]).

3.6.2 Energy-based nanoindentation approaches

Assuming that the fracture work (W_f) is equal to the critical plastic deformation work (W_p^*) that corresponds to a critical maximum indentation displacement (h_{max}^*) when fracture initiates [156], K_C of ductile material can be obtained by energy-based nanoindentation approach as [66]:
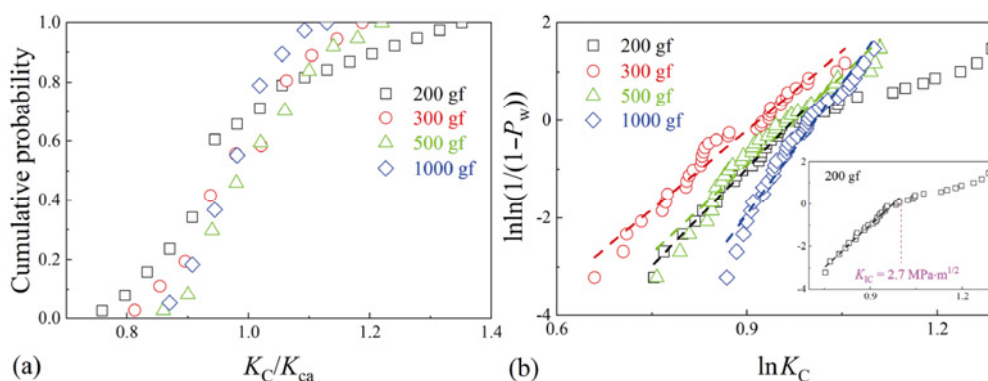

Fig. 13 Weibull analyses of fracture toughness of BST ceramic obtained by Vickers indenter-induced cracking method (K_C is calculated by Eq. (23)): (a) cumulative probability of normalized fracture toughness (i.e., K_C/K_{ca}); (b) Weibull plots of fracture toughness by Eq. (36).

Table 7 Statistical analysis results for measured K_C (MPa·m$^{1/2}$) of BST ceramic based on Vickers indenter-induced cracking method by Eq. (23)

P (gf)	K_C				Weibull parameter	
	K_{min}	K_{max}	K_{ca}	SD	K_{C_0}	m
200	2.1	3.6	2.5	0.4	2.6	13.3
300	1.9	2.9	2.3	0.2	2.5	10.8
500	2.1	3.0	2.5	0.2	2.6	13.1
1000	2.3	3.0	2.6	0.2	2.7	19.1

Note: K_{min}, K_{max}, K_{ca}, and SD are the minimum value, maximum value, arithmetic average, and standard deviation of values of K_C by Eq. (23), respectively.

$$K_C = \sqrt{G_C E_0} = \sqrt{E_0 \frac{W_p^*}{A_f^*}},$$

$$A_f^* = (h_{max}^*)^2 \left[\frac{\pi}{2} \tan^2 \alpha_B - \left(1 - \lambda \frac{H_{IT}}{E_r}\right) \tan \alpha_B \right] \quad (37)$$

where G_C is the critical strain energy release rate when fracture initiates; A_f^* is the critical contact area at h_{max}^*; and $\lambda = 4.52$ for Berkovich indenter, which also appears in Eq. (11). E_0 is the E_{IT} (E_{IT} can be calculated from E_r by Eq. (2)) measured by nanoindentation in the absence of indentation-induced damage under small loads. E_0 (= 260 GPa) is calculated by c_2 method (E_0 is just E_{IT} in Eq. (9)), since $E_r = 219$ GPa calculated by c_2

method lies within the range of E_r calculated by OP method (Eq. (2)) under small loads.

Figure 14(a) shows the variation of H_{IT} with E_r obtained by OP method (Eq. (2)). For large loads ($F_{max} > 120$ mN), H_{IT} increases with E_r in a linear way; H_{IT}/E_r increases with the increase in F_{max}, since E_r has a greater decline than H_{IT} under large F_{max}, as shown in Fig. 14(b); the larger H_{IT}/E_r under larger F_{max} is caused by indentation-induced damage. The proportional relationship between H_{IT} and E_r only holds under small loads ($F_{max} < 120$ mN), resulting in a constant value of H_{IT}/E_r in the absence of severe damage, which should be used to calculate fracture toughness by Eq. (37). Based on the proportional relationship between H_{IT}/E_r and W_e/W_t (= 0.46 (Fig. 7(a))), it can be calculated by Eq. (11) with $\chi = 0.174$ that $H_{IT}/E_r = 0.08$, which is a little larger than $H_{IT}/E_r = 0.075$ by curve fitting under small F_{max} (Fig. 14(a)). Since W_e/W_t is insensitive to indentation-induced damage, as shown in Fig. 7(a), $H_{IT}/E_r = 0.08$ calculated by the proportional relationship between H_{IT}/E_r and W_e/W_t by Eq. (11) is believed to be more reliable than H_{IT}/E_r obtained by OP method under small loads, which is subject to much uncertainty evidenced by the large data scatter due to surface effects [81,157].
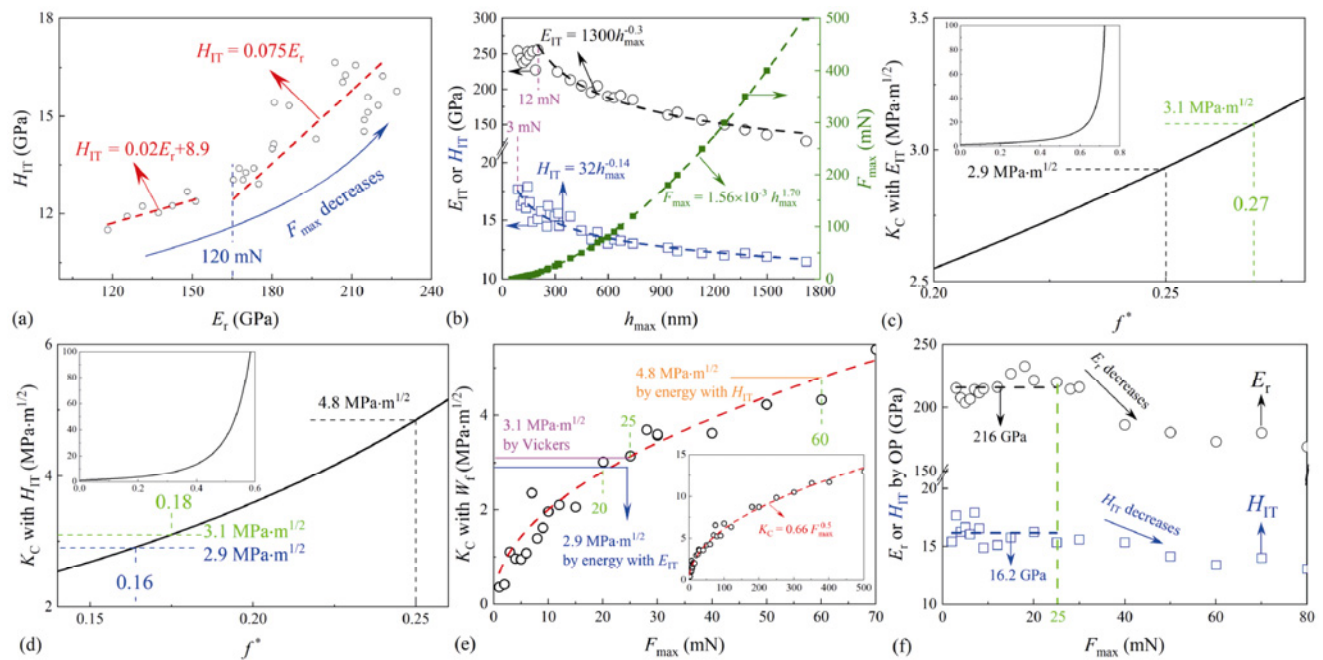
Figure 14(b) shows the variations of E_{IT} and H_{IT}

Fig. 14 Analysis of K_C of BST ceramic by energy-based nanoindentation approach: (a) variation of H_{IT} with E_r obtained by OP method (Eq. (2)); (b) dependence of E_{IT} and H_{IT} obtained by OP method (Eq. (2)) and F_{max} on h_{max}; dependence of K_C calculated by Eq. (41) on f^* based on deterioration of (c) E_{IT} and (d) H_{IT}; (e) variation of K_C calculated by Eq. (44) ($W_f = 0.09W_t$ for BST ceramic, and both E_r and A_p are obtained by OP method) with F_{max}; and (f) variations of E_r and H_{IT} by OP method (Eq. (2)) with F_{max}.

obtained by OP method with h_{max}. Both E_{IT} and H_{IT} nonlinearly decrease with the increase in h_{max} under large loads due to indentation-induced damage, and power-law functions are applicable to describe the decreasing trends. The data of H_{IT} under small F_{max} (< 3 mN) were not considered for curve fitting since indentation hardness is sensitive to many factors (e.g., surface condition and work hardening [108]), especially under small indentation depths. The data of E_{IT} under small F_{max} (< 12 mN) were not considered either for curve fitting, since a constant level of E_{IT}, which is insensitive to stress or strain state of material [32], can be approximated under small F_{max} (or h_{max}) in the absence of indentation-induced damage. The degradation (or deterioration) of E_{IT} and H_{IT} can be expressed as power-law functions of h_{max} under large loads in the presence of indentation-induced damage.

$$E_{IT} = 1300 h_{max}^{-0.3}, \quad H_{IT} = 32 h_{max}^{-0.14} \tag{38}$$

The critical total work (W_t^*) is obtained by integrating the loading curve, which can be expressed by $F = kh^n$, from zero point of contact to h_{max}^* [66].

$$W_t^* = \lim_{h \to h_{max}^*} \int_0^{h_{max}^*} F \mathrm{d}h$$
$$= \lim_{h \to h_{max}^*} \int_0^{h_{max}^*} kh^n \mathrm{d}h = \frac{k(h_{max}^*)^{n+1}}{n+1} \tag{39}$$

where k (= 1.56×10^{-3} mN/nm$^{1.7}$) and n (= 1.7) can be obtained by curve fitting of F_{max} vs. h_{max}, as shown in Fig. 14(b).

W_p^* can be determined by substituting Eq. (11) into Eq. (39) [66].

$$W_p^* = \left(1 - \frac{H_{IT}}{\chi E_r}\right) \frac{k(h_{max}^*)^{n+1}}{n+1} \tag{40}$$

Finally, K_C can be calculated by combining Eqs. (37) and (40).

$$K_C = \sqrt{E_0 \frac{1 - \dfrac{H_{IT}}{\chi E_r}}{\dfrac{\pi}{2}\tan^2\alpha_B - \left(1 - \lambda\dfrac{H_{IT}}{E_r}\right)^2 \tan\alpha_B} \frac{k(h_{max}^*)^{n-1}}{n+1}} \tag{41}$$

The critical indentation maximum displacement (h_{max}^*) can be determined by the critical damage variable (D^*) at fracture initiation. The deterioration of mechanical properties (e.g., indentation hardness and

elastic modulus) by material fracture can be characterized by damage variable (D) based on the continuum damage mechanics theory [137,138]:

$$D = 1 - \frac{H_{IT}}{H_0} \quad \text{or} \quad D = 1 - \frac{E_{IT}}{E_0} \tag{42}$$

where H_0 = 17.5 GPa is calculated by H_{IT}/E_r = 0.08 with E_r = 219 GPa, which is also used to calculated E_0. H_0 (= 17.5 GPa) is close to the values of H_{IT} obtained by OP method and c_2 method under small loads (Fig. 7(d)). D^* can be calculated by f^*.

$$D^* = \frac{\pi}{(4\pi/3)^{2/3}} (f^*)^{2/3} \tag{43}$$

where f^* = 0.25 is used for ductile materials [158–160], resulting in D^* = 0.48. With D^* = 0.48 and E_0 = 260 GPa (or H_0 = 17.5 GPa), H_{IT} and E_{IT} at fracture initiation can be determined by Eq. (42) to be E_{IT}^* = 135 GPa and H_{IT}^* = 9.1 GPa, respectively, and thus h_{max}^* can be obtained by Eq. (38) based on the data, as shown in Fig. 14(b). It is worth noting that E_{IT}^* and H_{IT}^* depend on D^* by Eq. (42), and different values of D^* result in different values of h_{max}^*, and a larger h_{max}^* results in a larger K_C by Eq. (41). Under D^* = 0.48 and E_{IT}^* = 135 GPa, it is found that h_{max}^* = 1888 nm by Eq. (38), which is close to h_{max} = 1721 nm at F_{max} = 500 mN, under which load cracking is observed (the inset of Fig. 4(a)). Nevertheless, under D^* = 0.48 and H_{IT}^* = 9.1 GPa, it is found that h_{max}^* = 7935 nm by Eq. (38), which is significantly larger than that obtained by E_{IT}^*, resulting in K_C obtained by H_{IT}^* being larger than that obtained by E_{IT}^*. It can be obtained by Eq. (41) that K_C = 2.9 MPa·m$^{1/2}$ at h_{max}^* = 1888 nm is only a little smaller than that obtained by Eq. (32) (i.e., 3.1 MPa·m$^{1/2}$) and lies within the reasonable range of 3–4 MPa·m$^{1/2}$ [142–145]; K_C = 4.8 MPa·m$^{1/2}$ at h_{max}^* = 7935 nm is a little larger than the value in reasonable range of fracture toughness of BST.

f^* = 0.25, which was proposed for ductile material [158–160], may not be suitable for brittle ceramics, and K_C calculated by Eq. (41) is dependent on the choice of f^*. E_{IT}^* and H_{IT}^* are related to f^* by substituting Eq. (43) into Eq. (42), and thus the relation between h_{max}^* and f^* can be obtained by Eq. (38), and finally K_C can be expressed as a function of f^* with Eq. (41). The dependence of K_C on f^* is displayed in

Figs. 14(c) and 14(d) based on the deterioration of E_{IT} and H_{IT}, respectively. Based on the deterioration of E_{IT}, $f^* = 0.27$ should be used for brittle ceramics, under which condition $K_C = 3.1$ MPa·m$^{1/2}$ by Eq. (41) is the same as the fracture toughness obtained by Vickers indenter-induced cracking method. $f^* = 0.25$ proposed for ductile material can also be used, since K_C is only a little underestimated based on the deterioration of E_{IT}. When the deterioration of H_{IT} is considered, $f^* = 0.18$ gives the same fracture toughness as that (i.e., $K_C = 3.1$ MPa·m$^{1/2}$) obtained by Vickers indenter-induced cracking method; and $f^* = 0.16$ leads to the same K_C (i.e., 2.9 MPa·m$^{1/2}$) obtained by the deterioration of E_{IT} with $f^* = 0.25$. Therefore, f^* should lie within the range from 0.16 to 0.18 for brittle ceramics if deterioration of H_{IT} is considered.

K_C can also be calculated from a single indentation test [67]:

$$K_C = \sqrt{\frac{W_f}{A_p(h_c)} E_r} \tag{44}$$

where E_r is obtained by OP method Eq. (2), as shown in Fig. 7(c) that E_r decreases with the increasing load under large F_{max}; W_f is a part of W_p, which is the sum of pure plastic work (W_{pp}) and W_f. The W_t can be expressed as [67]:

$$W_t = W_e + W_p = W_e + W_{pp} + W_f \tag{45}$$

where W_{pp} can be calculated by Eq. (46) [67,161]:

$$\frac{W_{pp}}{W_t} = 1 - \frac{1 - 3\left(\frac{h_p}{h_{max}}\right)^2 + 2\left(\frac{h_p}{h_{max}}\right)^3}{1 - \left(\frac{h_p}{h_{max}}\right)^2} \tag{46}$$

where $h_p/h_{max} = 0.62$, as shown in Fig. 5(a), resulting in $W_{pp} = 0.45W_t$, and $W_f = 0.55W_t - W_e$. Since $W_e = 0.46W_t$, as shown in Fig. 7(a), it can be computed that $W_f = 0.09W_t$ for BST ceramic.

The values of K_C calculated by Eq. (44) under different F_{max} are shown in Fig. 14(e). $K_C = 2.9$ and 4.8 MPa·m$^{1/2}$ by Eq. (41) with $f^* = 0.25$ based on the deterioration of E_{IT} and H_{IT}, respectively, and $K_C = 3.1$ MPa·m$^{1/2}$ obtained by Vickers indenter-induced cracking method by Eq. (32) are all included in Fig. 14(e) for comparison. K_C by Eq. (44) is nonlinearly dependent on F_{max}, which can be expressed by a power-law function: $K_C = 0.66\sqrt{F_{max}}$ (the units of

K_C and F_{max} are MPa·m$^{1/2}$ and mN, respectively). Reasonable values of fracture toughness (i.e., $K_C = 2.9$–3.1 MPa·m$^{1/2}$) can be calculated by Eq. (44) under 20 mN < F_{max} < 25 mN, and it is striking to note that both E_r and H_{IT} can be approximated to be constant for F_{max} < 25 mN and start decreasing apparently when F_{max} increases beyond 25 mN, which can be regarded to be the critical load for initiation of fracture, as shown in Fig. 14(f), showing the variations of E_r and H_{IT} under small F_{max} (< 80 mN). E_r and H_{IT} both decrease under large loads, which can be explained by noting that the surrounding voids or defects around the indented region can play an increasingly significant role as the load or contact area increases, resulting in indentation-induced cracking rather than the substrate effect for soft battery material studied under small loads in the absence of cracking damage [100], and the influence of differently colored regions of small sizes on mechanical properties of BST ceramic can be neglected under large loads. Reliable fracture toughness can be obtained by fracture energy-based approach (Eq. (44)) at the critical load of fracture initiation, which can be determined by the apparent decrease in E_r and H_{IT} under small F_{max}. For F_{max} < 25 mN in the absence of indentation-induced damage, E_r can be approximated to be a constant of 216 GPa, which is almost the same as $E_r = 219$ GPa obtained by c_2 method (Eq. (9)); H_{IT} can also be approximated to be a constant of 16.2 GPa, which is close to $H_0 = 17.5$ GPa (calculated by $H_{IT}/E_r = 0.08$ with $E_r = 219$ GPa) that is used as the indentation hardness without the effect of damage in Eq. (42).

The results by energy-based nanoindentation approaches are consistent with that measured by Eq. (32). The f^* used in calculation of fracture toughness by enery-based nanoindentation approaches (Eq. (41)) depends on whether deterioration of E_{IT} or H_{IT} is considered, and it is found for brittle ceramics $f^* = 0.27$ (or 0.18) if E_{IT} (or H_{IT}) is used. Fracture toughness of brittle ceramics can also be obtained by Eq. (44) at the critical load of fracture initiation, which is indicated by the lowest indentation load that makes H_{IT} or E_r start decreasing.

3.6.3 Scratch-based methodologies

With the assumption of emanation of a semi-circular horizontal crack plane in front of the indenter tip, as shown in Fig. 10, K_C can be estimated during scratching under axisymmetric indenters based on LEFM [68] and MESEL [69–71,162,163]:

$$\sigma_h = \frac{F_h}{S_h} =$$

$$\begin{cases} K_C / \sqrt{\Lambda}, & \text{for LEFM} \\ K_C / \sqrt{\Lambda_0 + \Lambda}, & \text{for Akono's ESEL} \\ K_C / \sqrt{\Lambda\left(1 + \dfrac{D_0}{d_p}\right)}, & \text{for Hubler and Ulm's ESEL} \\ K_C / \sqrt{d_p + c_f \dfrac{\Lambda}{d_p}}, & \text{for Liu's ESEL} \end{cases} \tag{47}$$

where D_0 represents the fracture process zone size; c_f can be used to estimate the length scale of cohesion zone of the tested material [71]; Λ_0 is a transitional length scale with the same order of magnitude of interface of heterogeneous material [70]; and $\Lambda\ (= S_h / 2l_p)$ is the nominal size. For Berkovich indenter, $\Lambda = \dfrac{\sqrt{3} d_p \tan \alpha_B}{4\sqrt{3\tan^2 \alpha_B + 1}}$, where $\alpha_B = 65.27°$, and $\Lambda\left(1 + \dfrac{D_0}{d_p}\right) = \Lambda + \dfrac{\sqrt{3} D_0 \tan \alpha_B}{4\sqrt{3\tan^2 \alpha_B + 1}}$ for Hubler and Ulm's ESEL.

Figure 15 shows that σ_h decreases with the increase in Λ or d_p for Berkovich and spherical indenters. Indenter geometry plays a significant role in scratch-induced cracking: The fluctuation and instability of σ_h for Berkovich indenter, as shown in Figs. 15(a) and 15(b), are attributed to cracking and damage induced by the sharp edge of the indenter (Fig. 9(a)); while the variations of σ_h and d_p for a spherical indenter are smoother, as shown in Figs. 15(c) and 15(d), respectively, since surface damage is slight, as shown in Fig. 9(b). The values of K_C obtained by LEFM, Akono's ESEL, and Hubler and Ulm's ESEL are more or less the same, which can be explained by noting that the fitting parameters (Λ_0 and D_0) in Akono's ESEL and Hubler and Ulm's ESEL, respectively, are negligibly small, and can be regarded to be zero for both Berkovich and spherical indenters, under which condition Akono's ESEL and Hubler and Ulm's ESLS are reduced to LEFM model, indicating that LEFM is suitable for assessing fracture toughness of brittle materials like ceramics and glasses [164]. $K_C = 3.03$ MPa·m$^{1/2}$ obtained by LEFM under a spherical indenter lies within the reasonable range (i.e., 3–4 MPa·m$^{1/2}$) [142–144], and is almost the same as those measured by Vickers indenter-induced cracking method (i.e., $K_C = 3.1$ MPa·m$^{1/2}$) and energy-based nanoindentation approach ($K_C = 3.1$ MPa·m$^{1/2}$ with the deterioration of E_{IT} under $f^* = 0.27$).
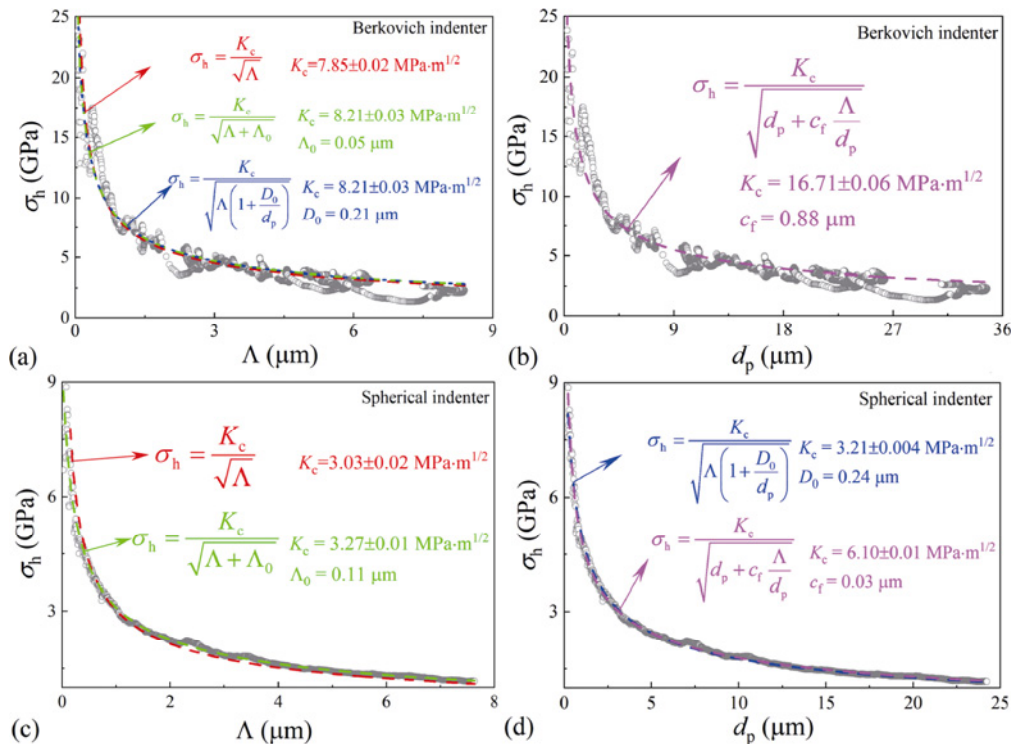

Fig. 15 Analyses of K_C of BST ceramic by different scratch-based approaches (e.g., LEFM, Akono's ESEL, Hubler and Ulm's ESEL, and Liu's ESEL) in Eq. (47) for (a, b) Berkovich indenter and (c, d) spherical indenter.

K_C = 7.9 MPa·m$^{1/2}$ obtained by LEFM under Berkovich indenter is about twice the reasonable value, which can be explained by noting that the assumption of a semi-circular horizontal crack plane emanating from the indenter tip does not hold for Berkovich indenter, which can cause severe damage and complex cracking; scratch-based approaches (Eq. (47)) were proposed for axisymmetric indenters rather than Berkovich indenter lacking axial symmetry. Modification of Eq. (47) is necessary when Berkovich indenter is applied to measure fracture toughness, and a simple modification of LEFM gives $\sigma_h = 2K_C / \sqrt{\Lambda}$ for Berkovich indenter. Values of K_C obtained by Liu's ESEL under a spherical indenter is 6.1 MPa·m$^{1/2}$, which also lies within the range (i.e., 2–7 MPa·m$^{1/2}$) of ceramics and ceramic composites measured by single edge V-notched and pre-cracked beam methods [22,23] or Vickers indenter-induced cracking method [12,13]. Values of K_C obtained by Liu's ESEL are about twice those obtained by LEFM for both spherical and Berkovich indenters, and K_C obtained by Liu's ESEL can be regarded to be the fracture toughness measured under plane stress condition, which is larger than that measured under plain strain condition [165]. A simple modification of Liu's ESEL can also render fracture toughness close to that obtained by LEFM, and $\sigma_h =$

$2K_C \Big/ \sqrt{d_p + c_f \dfrac{\Lambda}{d_p}}$ for the modified Liu's ESEL.

Therefore, LEFM by a spherical indenter provides the most suitable scratch-based approach to calculate fracture toughness of brittle BST ceramic. LEFM model, Akono's MESEL model, and Hubler's MESEL model, which have been successfully applied to characterize the fracture toughness of materials of low fracture toughness (e.g., glasses, ceramics, and polymers), might not be suitable for metallic materials of high fracture toughness, and Liu's MESEL model is more suitable to characterize metals of large fracture toughness [166].

The reasonable and consistent values of fracture toughness can be obtained by Vickers indenter-induced cracking method (Eq. (32)), energy-based nanoindentation approaches with Berkovich indenter (Eqs. (41) and (44)), and LEFM-based scratch approach with a spherical indenter (Eq. (47)). Vickers indenter-induced cracking method requires many repeated tests under the same load, nanoindentation approaches require many tests under various loads, while a continuously

increasing load can be used, and fracture toughness can be calculated in a single scratch test, and thus scratch approach with a spherical indenter provides the most efficient means to estimate fracture toughness of brittle ceramics.

4   Conclusions

Micromechanical properties of BST ceramic were characterized by nanoindentation, microhardness, and microscratch tests. The elastic modulus and indentation hardness were analyzed by OP method, c_2 method, Cheng theory, Gong theory, energy-based approach, and displacement-based approach. The elastic modulus was also calculated by resonant ultrasound spectroscopy and the elastic recovery of Knoop imprint. Elastic modulus and indentation hardness of brittle ceramics should be measured under low loads with little influence of indentation-induced cracking, and c_2 method and OP method can be used to characterize the elastic modulus (i.e., 260 GPa) and indentation hardness (i.e., 16.2 GPa) of brittle BST ceramic based on the data under small loads. The much significant fluctuation of lateral force during scratch test under Berkovich indenter compared to that under a spherical indenter indicates that severe surface damage can be induced by the sharp Berkovich indenter, while surface is slightly damaged with a large elastic recovery due to the blunt tip of a spherical indenter. Three different regimes during scratch can be determined based on the variations of penetration depth, residual depth, and scratch friction coefficient. The microstructures of BST ceramic were characterized by the XRD, SEM, and Raman spectra.

Consistent values of fracture toughness (i.e., 3.0 MPa·m$^{1/2}$ within the reasonable range of 3–4 MPa·m$^{1/2}$) of BST ceramic can be estimated by various methods such as Vickers indenter-induced cracking method, energy-based nanoindentation approaches with Berkovich indenter, and LEFM-based scratch approach with a spherical indenter. For calculation of fracture toughness of brittle ceramics by energy-based nanoindentation approaches, $f^* = 0.27$, which is close to 0.25 proposed for the ductile material, can be used when the deterioration of elastic modulus is considered; while $f^* = 0.18$ should be used when the deterioration of indentation hardness is considered. Fracture toughness can be obtained by fracture work-based approach at a

critical load that corresponds to the initiation of fracture identified by the initial decrease in elastic modulus and indentation hardness. Scratch approach with a spherical indenter provides the most efficient means to estimate fracture toughness of brittle ceramics, since various loads can be progressively applied in a single scratch test.

Acknowledgements

Declaration of competing interest

The authors have no competing interests to declare that are relevant to the content of this article.

References

[1] Toktas A, Ustun D, Tekbas M. Global optimization scheme based on triple-objective ABC algorithm for designing fully optimized multi-layer radar absorbing material. *IET Microw Antenna P* 2020, **14**: 800–811.

[2] Zhou X, Liu LT, Sun JJ, *et al*. Effects of $(Mg_{1/3}Sb_{2/3})^{4+}$ substitution on the structure and microwave dielectric properties of $Ce_2Zr_3(MoO_4)_9$ ceramics. *J Adv Ceram* 2021, **10**: 778–789.

[3] Feng C, Zhou X, Tao BJ, *et al*. Crystal structure and enhanced microwave dielectric properties of the $Ce_2[Zr_{1-x}(Al_{1/2}Ta_{1/2})_x]_3(MoO_4)_9$ ceramics at microwave frequency. *J Adv Ceram* 2022, **11**: 392–402.

[4] Zhou L, Qiu JY, Wang XG, *et al*. Mechanical and dielectric properties of reduced graphene oxide nanosheets/alumina composite ceramics. *Ceram Int* 2020, **46**: 19731–19737.

[5] Duan WJ, Yang ZH, Cai DL, *et al*. Effect of sintering temperature on microstructure and mechanical properties of boron nitride whisker reinforced fused silica composites. *Ceram Int* 2020, **46**: 5132–5140.

[6] Li RR, Li YM, Yan CY, *et al*. Thickness-dependent and tunable mechanical properties of $CaTiO_3$ dielectric thin films determined by nanoindentation technique. *Ceram Int* 2020, **46**: 22643–22649.

[7] Liu M, Xu ZT, Fu RL. Micromechanical and microstructure characterization of $BaO–Sm_2O_3–5TiO_2$ ceramic with addition of Al_2O_3. *Ceram Int* 2022, **48**: 992–1005.

[8] Sikder AK, Irfan IM, Kumar A, *et al*. Nano-indentation studies of xerogel and SiLK low-*K* dielectric materials. *J Electron Mater* 2001, **30**: 1527–1531.

[9] Zheng ZW, Sridhar I, Balakumar S. A comparative study on the measurement of toughness of stacks containing low-*K* dielectric films. *Microelectron Eng* 2008, **85**: 2322–2328.

[10] Singh L, Sheeraz M, Chowdhury MN, *et al*. Investigation of dielectric, mechanical, and electrical properties of flame synthesized $Y_{2/3}Cu_{2.90}Zn_{0.10}Ti_4O_{12}$ material. *J Mater Sci Mater Electron* 2018, **29**: 10082–10091.

[11] Ding ZD, Ridley M, Deijkers J, *et al*. The thermal and mechanical properties of hafnium orthosilicate: Experiments and first-principles calculations. *Materialia* 2020, **12**: 100793.

[12] Zhao DK, Wu DJ, Shi J, *et al*. Microstructure and mechanical properties of melt-grown alumina–mullite/glass composites fabricated by directed laser deposition. *J Adv Ceram* 2022, **11**: 75–93.

[13] Chen L, Li BH, Guo J, *et al*. High-entropy perovskite $RETa_3O_9$ ceramics for high-temperature environmental/thermal barrier coatings. *J Adv Ceram* 2022, **11**: 556–569.

[14] Tesař K, Maňák J, Vaněk P, *et al*. Microstructure and micromechanical properties of GaV_4S_8 ceramics prepared by single-step solid state synthesis. *Ceram Int* 2020, **46**: 7045–7049.

[15] Warangkanagool C. Physical, dielectric properties and micro-hardness of the $(Ba_{0.90}Ca_{0.10})_{0.90}(Na_{0.50}Bi_{0.50})_{0.10}TiO_3$ ceramics prepared by molten salt method. *Solid State Phenom* 2018, **283**: 132–139.

[16] Takahashi J, Ikegami T, Kageyama K. Occurrence of dielectric 1 : 1 : 4 compound in the ternary system $BaO–Ln_2O_3–TiO_2$ (Ln = La, Nd, and Sm): II, Reexamination of formation of isostructural ternary compounds in identical systems. *J Am Ceram Soc* 1991, **74**: 1873–1879.

[17] Chen GH, Di JC, Xu HR, *et al*. Microwave dielectric properties of $Ca_4La_2Ti_{5-x}(Mg_{1/3}Nb_{2/3})_xO_{17}$ ceramics. *J Am Ceram Soc* 2012, **95**: 1394–1397.

[18] Xu Y, Fu RL, Agathopoulos S, *et al*. Synthesis and microwave dielectric properties of $BaO–Sm_2O_3–5TiO_2$ ceramics with $NdAlO_3$ additions. *Ceram Int* 2016, **42**: 14573–14580.

[19] Guo WJ, Ma ZY, Luo Y, *et al*. Structure, defects, and microwave dielectric properties of Al-doped and Al/Nd co-doped $Ba_4Nd_{9.33}Ti_{18}O_{54}$ ceramics. *J Adv Ceram* 2022, **11**: 629–640.

[20] Adamczyk M, Kozielski L, Pawełczyk M, *et al*. Dielectric and mechanical properties of $BaBi_2(Nb_{0.99}V_{0.01})_2O_9$ ceramics. *Arch Metall Mater* 2011, **56**: 1163–1168.

[21] Guiu F, Hahn BS, Lee HL, *et al*. Growth of indentation cracks in poled and unpoled PZT. *J Eur Ceram Soc* 1997, **17**: 505–512.

[22] Qiu BF, Duan XM, Zhang Z, *et al*. Microstructural evolution of h-BN matrix composite ceramics with La–Al–Si–O

glass phase during hot-pressed sintering. *J Adv Ceram* 2021, **10**: 493–501.

[23] Chen SN, Fan HZ, Su YF, *et al*. Influence of binder systems on sintering characteristics, microstructures, and mechanical properties of PcBN composites fabricated by SPS. *J Adv Ceram* 2022, **11**: 321–330.

[24] Gong JH. Microstructural effects in brittle fracture of ceramics. *Adv Ceram* 2021, **42**: 287–428. (in Chinese)

[25] Long X, Jia QP, Shen ZY, *et al*. Strain rate shift for constitutive behaviour of sintered silver nanoparticles under nanoindentation. *Mech Mater* 2021, **158**: 103881.

[26] Li Y, Liu YZ, Wang R. Evaluation of the elastic modulus of concrete based on indentation test and multi-scale homogenization method. *J Build Eng* 2021, **43**: 102758.

[27] Fu HY, Cai LX, Chai ZJ, *et al*. Evaluation of bonding properties by flat indentation method for an EBW joint of RAFM steel for fusion application. *Nucl Mater Energy* 2020, **25**: 100861.

[28] Chen H, Cai LX, Bao C. Equivalent-energy indentation method to predict the tensile properties of light alloys. *Mater Design* 2019, **162**: 322–330.

[29] Zhang Z, Liu M, Tu HY, *et al*. Nanoindentation creep behaviour and microstructural evolution of long-term crept HR3C austenitic steel. *Mater High Temp* 2021, **38**: 403–416.

[30] Liu M, Ren TL, Gao CH. Correspondence relationship between the maximum tensile stress and cycle number during the initial stage of low-cycle fatigue test. *J Test Eval* 2021, **49**: 1570–1585.

[31] Islam MM, Shakil SI, Shaheen NM, *et al*. An overview of microscale indentation fatigue: Composites, thin films, coatings, and ceramics. *Micron* 2021, **148**: 103110.

[32] Liu M, Zheng Q, Wang X, *et al*. Characterization of distribution of residual stress in shot-peened layer of nickel-based single crystal superalloy DD6 by nanoindentation technique. *Mech Mater* 2022, **164**: 104143.

[33] Yu F, Fang J, Omacht D, *et al*. A new instrumented spherical indentation test methodology to determine fracture toughness of high strength steels. *Theor Appl Fract Mech* 2023, **124**: 103744.

[34] Schlech T, Horn S, Wijayawardhana C, *et al*. Experimental and FEM based investigation of the influence of the deposition temperature on the mechanical properties of SiC coatings. *J Adv Ceram* 2021, **10**: 139–151.

[35] Zhao GF, Liu M, Yang FQ. The effect of an electric current on the nanoindentation behavior of tin. *Acta Mater* 2012, **60**: 3773–3782.

[36] Gao CH, Liu M. Characterization of spherical indenter with fused silica under small deformation by Hertzian relation and Oliver and Pharr's method. *Vacuum* 2018, **153**: 82–90.

[37] Liu M, Hou DY, Gao CH. Berkovich nanoindentation of $Zr_{55}Cu_{30}Al_{10}Ni_5$ bulk metallic glass at a constant loading rate. *J Non-Cryst Solids* 2021, **561**: 120750.

[38] Gong JH. Theoretical foundation and data analyses of quasi-static nanoindentation. *J Ceram* 2021, **42**: 181–245. (in Chinese)

[39] Gao CH, Liu M. Power law creep of polycarbonate by Berkovich nanoindentation. *Mater Res Express* 2017, **4**: 105302.

[40] Li S, Zhang JH, Liu M, *et al*. Influence of polyethyleneimine functionalized graphene on tribological behavior of epoxy composite. *Polym Bull* 2021, **78**: 6493–6515.

[41] Li HZ, Chen JL, Chen QR, *et al*. Determining the constitutive behavior of nonlinear visco–elastic–plastic PMMA thin films using nanoindentation and finite element simulation. *Mater Design* 2021, **197**: 109239.

[42] Liu M, Yang FQ. Finite element analysis of the spherical indentation of transversely isotropic piezoelectric materials. *Model Simul Mater Sc* 2012, **20**: 045019.

[43] Liu M, Yang FQ. Finite element simulation of the effect of electric boundary conditions on the spherical indentation of transversely isotropic piezoelectric films. *Smart Mater Struct* 2012, **21**: 105020.

[44] Liu M, Yang FQ. Orientation effect on the Boussinesq indentation of a transversely isotropic piezoelectric material. *Int J Solids Struct* 2013, **50**: 2542–2547.

[45] Liu M, Yang FQ. Three-dimensional finite element simulation of the Berkovich indentation of a transversely isotropic piezoelectric material: Effect of material orientation. *Model Simul Mater Sc* 2013, **21**: 045014.

[46] Liu M, Yang FQ. Finite element analysis of the indentation-induced delamination of Bi-layer structures. *J Comput Theor Nanos* 2012, **9**: 851–858.

[47] Liu M. Finite element analysis of effects of mechanical properties on indentation-induced interfacial delamination. *J Comput Theor Nanos* 2014, **11**: 1697–1706.

[48] Liu M, Yang FQ. Indentation-induced interface decohesion between a piezoelectric film and an elastic substrate. *J Comput Theor Nanos* 2014, **11**: 1863–1873.

[49] Yang FQ, Liu M. Analysis for the indentation with a flat indenter on an elastic-perfectly plastic thin film. *J Comput Theor Nanos* 2014, **11**: 265–271.

[50] Zheng KK, Gao CH, He FS, *et al*. Study on the interfacial functionary mechanism of rare-earth-solution-modified bamboo-fiber-reinforced resin matrix composites. *Materials* 2018, **11**: 1190.

[51] Liu M, Yan FW, Gao CH. Effect of sliding velocity of a spherical indenter on microscratch response of materials. *J Fuzhou Univ* 2021, **49**: 473–484. (in Chinese)

[52] Buijnsters JG, Shankar P, van Enckevort WJP, *et al*. Adhesion analysis of polycrystalline diamond films on molybdenum by means of scratch, indentation and sand abrasion testing. *Thin Solid Films* 2005, **474**: 186–196.

[53] Mendas M, Benayoun S. Investigating the effects of microstructure on the wear mechanisms in lamellar cast irons via microscratch tests. *Tribol Int* 2013, **67**: 124–131.

[54] Yang ACM, Wu TW. Wear and friction in glassy

polymers: Microscratch on blends of polystyrene and poly(2,6-dimethyl-1,4-phenylene oxide). *J Polym Sci Pol Phys* 1997, **35**: 1295–1309.

[55] Liu M, Zheng Q, Gao CH. Sliding of a diamond sphere on fused silica under ramping load. *Mater Today Commun* 2020, **25**: 101684.

[56] Kleinbichler A, Pfeifenberger MJ, Zechner J, *et al*. Scratch induced thin film buckling for quantitative adhesion measurements. *Mater Design* 2018, **155**: 203–211.

[57] Ctibor P, Sedláček J, Hudec T. Dielectric properties of Ce-doped YAG coatings produced by two techniques of plasma spraying. *Bol Soc Esp Ceram V* 2022, **61**: 408–416.

[58] Gao CH, Liu M. Instrumented indentation of fused silica by Berkovich indenter. *J Non-Cryst Solids* 2017, **475**: 151–160.

[59] Gong JH, Miao HZ, Peng ZJ. Analysis of the nanoindentation data measured with a Berkovich indenter for brittle materials: Effect of the residual contact stress. *Acta Mater* 2004, **52**: 785–793.

[60] Cheng YT, Cheng CM. Relationships between hardness, elastic modulus, and the work of indentation. *Appl Phys Lett* 1998, **73**: 614–616.

[61] Cheng YT, Li ZY, Cheng CM. Scaling relationships for indentation measurements. *Philos Mag A* 2002, **82**: 1821–1829.

[62] Cheng YT, Cheng CM. Scaling, dimensional analysis, and indentation measurements. *Mater Sci Eng* 2004, **44**: 91–149.

[63] Gong JH, Deng B, Jiang DY. A universal function for the description of nanoindentation unloading data: Case study on soda-lime glass. *J Non-Cryst Solids* 2020, **544**: 120067.

[64] Gao CH, Yao LG, Liu M. Berkovich nanoindentation of borosilicate K9 glass. *Opt Eng* 2018, **57**: 034104.

[65] Marshall DB, Noma T, Evans AG. A simple method for determining elastic-modulus-to-hardness ratios using Knoop indentation measurements. *J Am Ceram Soc* 1982, **65**: c175–c176.

[66] Guo H, Jiang CB, Yang BJ, *et al*. On the fracture toughness of bulk metallic glasses under Berkovich nanoindentation. *J Non-Cryst Solids* 2018, **481**: 321–328.

[67] Yang ZN, Wang LM, Chen ZW, *et al*. Micromechanical characterization of fluid/shale interactions by means of nanoindentation. *SPE Reserv Eval Eng* 2018, **21**: 405–417.

[68] Barenblatt GI. The mathematical theory of equilibrium cracks in brittle fracture. *Adv Appl Mech* 1962, **7**: 55–129.

[69] Hubler MH, Ulm FJ. Size-effect law for scratch tests of axisymmetric shape. *J Eng Mech* 2016, **142**: 04016094.

[70] Akono AT. Energetic size effect law at the microscopic scale: Application to progressive-load scratch testing. *J Nanomech Micromech* 2016, **6**: 04016001.

[71] Zhang D, Sun Y, Gao CH, *et al*. Measurement of fracture toughness of copper via constant-load microscratch with a spherical indenter. *Wear* 2020, **444–445**: 203158.

[72] Fischer-Cripps AC. *Nanoindentation*, 3rd edn. New York, USA: Springer New York, 2011.

[73] Tao K, Khonik VA, Qiao JC. Indentation creep dynamics in metallic glasses under different structural states. *Int J Mech Sci* 2023, **240**: 107941.

[74] Gao CH, Liu M. Effects of normal load on the coefficient of friction by microscratch test of copper with a spherical indenter. *Tribol Lett* 2019, **67**: 8.

[75] Liu M. Influence of sample tilt and applied load on microscratch behavior of copper under a spherical diamond indenter. *Tribol Lett* 2021, **69**: 88.

[76] Liu M, Huang CX, Gao CH. Effect of sample tilt and normal load on micro-scratch test of copper with a spherical indenter. *Tribology* 2021, **41**: 27–37. (in Chinese)

[77] Gao CH, Yao LG, Liu M. Measurement of sample tilt by residual imprint morphology of Berkovich indenter. *J Test Eval* 2020, **48**: 20180136.

[78] Gadelrab KR, Bonilla FA, Chiesa M. Densification modeling of fused silica under nanoindentation. *J Non-Cryst Solids* 2012, **358**: 392–398.

[79] Choi Y, Lee HS, Kwon D. Analysis of sharp-tip-indentation load–depth curve for contact area determination taking into account pile-up and sink-in effects. *J Mater Res* 2004, **19**: 3307–3315.

[80] Durst K, Backes B, Franke O, *et al*. Indentation size effect in metallic materials: Modeling strength from pop-in to macroscopic hardness using geometrically necessary dislocations. *Acta Mater* 2006, **54**: 2547–2555.

[81] Zhang TY, Xu WH. Surface effects on nanoindentation. *J Mater Res* 2002, **17**: 1715–1720.

[82] Mata M, Alcalá J. The role of friction on sharp indentation. *J Mech Phys Solids* 2004, **52**: 145–165.

[83] Moseson AJ, Basu S, Barsoum MW. Determination of the effective zero point of contact for spherical nanoindentation. *J Mater Res* 2008, **23**: 204–209.

[84] Zong WJ, Wu D, He CL. Radius and angle determination of diamond Berkovich indenter. *Measurement* 2017, **104**: 243–252.

[85] Yang HC, Zhang SR, Yang HY, *et al*. The latest process and challenges of microwave dielectric ceramics based on pseudo phase diagrams. *J Adv Ceram* 2021, **10**: 885–932.

[86] Čelko L, Gutiérrez-Cano V, Casas-Luna M, *et al*. Characterization of porosity and hollow defects in ceramic objects built by extrusion additive manufacturing. *Addit Manuf* 2021, **47**: 102272.

[87] Safarzadeh M, Chee CF, Ramesh S, *et al*. Effect of sintering temperature on the morphology, crystallinity and mechanical properties of carbonated hydroxyapatite (CHA). *Ceram Int* 2020, **46**: 26784–26789.

[88] Wu SY, Li Y, Chen XM. Raman spectra of $Ba_{6-3x}Sm_{8+2x}Ti_{18}O_{54}$ solid solution. *J Phys Chem Solids* 2003, **64**: 2365–2368.

[89] Randall NX, Vandamme M, Ulm FJ. Nanoindentation analysis as a two-dimensional tool for mapping the mechanical properties of complex surfaces. *J Mater Res* 2009, **24**: 679–690.

[90] Vandamme M, Ulm FJ. Nanogranular origin of concrete creep. *PNAS* 2009, **106**: 10552–10557.

[91] Jiang JD, Shen JY, Hou DW. Determination of fracture toughness of hydrated calcium silicate by nanoindentation. *J Chin Ceram Soc* 2018, **46**: 1067–1073. (in Chinese)

[92] Liu M, Xu ZT, Gao CH. Determination of mechanical properties of microstructure in metals based on grid nanoindentation. *J Fuzhou Univ* 2021, **49**: 797–808 (in Chinese).

[93] De Vasconcelos LS, Xu R, Li JL, *et al*. Grid indentation analysis of mechanical properties of composite electrodes in Li-ion batteries. *Extreme Mech Lett* 2016, **9**: 495–502.

[94] Ulm FJ, Vandamme M, Bobko C, *et al*. Statistical indentation techniques for hydrated nanocomposites: Concrete, bone, and shale. *J Am Ceram Soc* 2007, **90**: 2677–2692.

[95] Cała M, Cyran K, Kawa M, *et al*. Identification of microstructural properties of shale by combined use of X-ray micro-CT and nanoindentation tests. *Procedia Eng* 2017, **191**: 735–743.

[96] Liu KQ, Ostadhassan M, Bubach B, *et al*. Statistical grid nanoindentation analysis to estimate macro-mechanical properties of the Bakken Shale. *J Nat Gas Sci Eng* 2018, **53**: 181–190.

[97] Constantinides G, Ulm FJ. The effect of two types of C–S–H on the elasticity of cement-based materials: Results from nanoindentation and micromechanical modeling. *Cement Concrete Res* 2004, **34**: 67–80.

[98] Constantinides G, Ulm FJ. The nanogranular nature of C–S–H. *J Mech Phys Solids* 2007, **55**: 64–90.

[99] Nohava J, Haušild P, Houdková Š, *et al*. Comparison of isolated indentation and grid indentation methods for HVOF sprayed cermets. *J Therm Spray Tech* 2012, **21**: 651–658.

[100] Sedlatschek T, Krämer M, Gibson JSKL, *et al*. Mechanical properties of heterogeneous, porous LiFePO$_4$ cathodes obtained using statistical nanoindentation and micromechanical simulations. *J Power Sources* 2022, **539**: 231565.

[101] Yoo BG, Choi IC, Kim YJ, *et al*. Room-temperature anelasticity and viscoplasticity of Cu–Zr bulk metallic glasses evaluated using nanoindentation. *Mater Sci Eng* 2013, **577**: 101–104.

[102] Oliver WC, Pharr GM. An improved technique for determining hardness and elastic modulus using load and displacement sensing indentation experiments. *J Mater Res* 1992, **7**: 1564–1583.

[103] Maiti P, Bhattacharya M, Das PS, *et al*. Indentation size effect and energy balance issues in nanomechanical behavior of ZTA ceramics. *Ceram Int* 2018, **44**: 9753–9772.

[104] Bolshakov A, Pharr GM. Influences of pileup on the measurement of mechanical properties by load and depth sensing indentation techniques. *J Mater Res* 1998, **13**: 1049–1058.

[105] Dao M, Chollacoop N, van Vliet KJ, *et al*. Computational modeling of the forward and reverse problems in instrumented sharp indentation. *Acta Mater* 2001, **49**: 3899–3918.

[106] Hays C, Kendall EG. An analysis of Knoop microhardness. *Metallography* 1973, **6**: 275–282.

[107] Jiang DY. Recent progresses in the phenomenological description for the indentation size effect in microhardness testing of brittle ceramics. *J Adv Ceram* 2012, **1**: 38–49.

[108] Gerk AP. The effect of work-hardening upon the hardness of solids: Minimum hardness. *J Mater Sci* 1977, **12**: 735–738.

[109] Ben Ghorbal G, Tricoteaux A, Thuault A, *et al*. Comparison of conventional Knoop and Vickers hardness of ceramic materials. *J Eur Ceram Soc* 2017, **37**: 2531–2535.

[110] Ben Ghorbal G, Tricoteaux A, Thuault A, *et al*. Mechanical characterization of brittle materials using instrumented indentation with Knoop indenter. *Mech Mater* 2017, **108**: 58–67.

[111] Riester L, Blau PJ, Lara-Curzio E, *et al*. Nanoindentation with a Knoop indenter. *Thin Solid Films* 2000, **377–378**: 635–639.

[112] Gong JH, Guan ZD. Fracture from Knoop indentation-induced flaws in sintered silicon carbide and hot-pressed silicon nitride. *Key Eng Mater* 2002, **224–226**: 765–770.

[113] Liu M, Zheng Q, Gao CH. Characterization of mechanical properties of bulk metallic glasses based on Knoop hardness. *Chinese J Solid Mech* 2021, **42**: 376–392. (in Chinese)

[114] Xie ZH, Hoffman M, Moon RJ, *et al*. Scratch damage in ceramics: Role of microstructure. *J Am Ceram Soc* 2003, **86**: 141–148.

[115] Yang XJ, Liu H, Luo L, *et al*. Experimental study on micro-nano scale cutting characteristics of single crystal germanium. *Chinese J Nonferrous Met* 2019, **29**: 1457–1465 (in Chinese).

[116] Luo L, Yang XJ. Mechanical properties experiment of monocrystalline germanium with multiple scratches based on nano scratch instrument. *Chinese J Nonferrous Met* 2019, **29**: 2341–2347 (in Chinese).

[117] Petit F, Ott C, Cambier F. Multiple scratch tests and surface-related fatigue properties of monolithic ceramics and soda lime glass. *J Eur Ceram Soc* 2009, **29**: 1299–1307.

[118] Lafaye S, Troyon M. On the friction behaviour in nanoscratch testing. *Wear* 2006, **261**: 905–913.

[119] Brookes CA, Moxley B. A pentagonal indenter for hardness measurements. *J Phys E Sci Instrum* 1975, **8**: 456–460.

[120] Ullner C, Germak A, Le Doussal H, *et al*. Hardness testing on advanced technical ceramics. *J Eur Ceram Soc* 2001, **21**: 439–451.

[121] Ullner C, Beckmann J, Morrell R. Instrumented indentation test for advanced technical ceramics. *J Eur Ceram Soc* 2002, **22**: 1183–1189.

[122] Chicot D, Mercier D, Roudet F, *et al*. Comparison of instrumented Knoop and Vickers hardness measurements on various soft materials and hard ceramics. *J Eur Ceram Soc* 2007, **27**: 1905–1911.

[123] Gong JH, Chen YF, Li CY. Statistical analysis of fracture

toughness of soda-lime glass determined by indentation. *J Non-Cryst Solids* 2001, **279**: 219–223.

[124] Quinn GD, Bradt RC. On the Vickers indentation fracture toughness test. *J Am Ceram Soc* 2007, **90**: 673–680.

[125] Blamey JM, Parry TV. Strength and toughness of barium titanate ceramics. *J Mater Sci* 1993, **28**: 4988–4993.

[126] Henry R, Le Roux N, Zacharie-Aubrun I, *et al*. Indentation cracking in mono and polycrystalline cubic zirconia: Methodology of an apparent fracture toughness evaluation. *Mater Sci Eng* 2022, **860**: 144261.

[127] Evans AG, Wilshaw TR. Quasi-static solid particle damage in brittle solids—I. Observations analysis and implications. *Acta Metall* 1976, **24**: 939–956.

[128] Ogilvy IM, Perrott CM, Suiter JW. On the indentation fracture of cemented carbide Part 1—Survey of operative fracture modes. *Wear* 1977, **43**: 239–252.

[129] Niihara K, Morena R, Hasselman DPH. Evaluation of K_{IC} of brittle solids by the indentation method with low crack-to-indent ratios. *J Mater Sci Lett* 1982, **1**: 13–16.

[130] Niihara K. A fracture mechanics analysis of indentation-induced Palmqvist crack in ceramics. *J Mater Sci Lett* 1983, **2**: 221–223.

[131] Lawn BR, Evans AG, Marshall DB. Elastic/plastic indentation damage in ceramics: The median/radial crack system. *J Am Ceram Soc* 1980, **63**: 574–581.

[132] Laugier MT. New formula for indentation toughness in ceramics. *J Mater Sci Lett* 1987, **6**: 355–356.

[133] Shetty DK, Wright IG, Mincer PN, *et al*. Indentation fracture of WC–Co cermets. *J Mater Sci* 1985, **20**: 1873–1882.

[134] Lawn BR, Swain MV. Microfracture beneath point indentations in brittle solids. *J Mater Sci* 1975, **10**: 113–122.

[135] Tanaka K. Elastic/plastic indentation hardness and indentation fracture toughness: The inclusion core model. *J Mater Sci* 1987, **22**: 1501–1508.

[136] Lawn BR, Fuller ER. Equilibrium penny-like cracks in indentation fracture. *J Mater Sci* 1975, **10**: 2016–2024.

[137] Evans AG, Charles EA. Fracture toughness determinations by indentation. *J Am Ceram Soc* 1976, **59**: 371–372.

[138] Anstis GR, Chantikul P, Lawn BR, *et al*. A critical evaluation of indentation techniques for measuring fracture toughness: I, Direct crack measurements. *J Am Ceram Soc* 1981, **64**: 533–538.

[139] Evans AG. Fracture toughness: The role of indentation techniques. In: *Fracture Mechanics Applied to Brittle Materials*. Freiman SW, Ed. West Conshohocken, USA: ASTM International, 1979: 112–135.

[140] Lankford J. Indentation microfracture in the Palmqvist crack regime: Implications for fracture toughness evaluation by the indentation method. *J Mater Sci Lett* 1982, **1**: 493–495.

[141] Blendell JE. The origins of internal stresses in polycrystalline Al_2O_3 and their effects on mechanical properties. Ph.D. Thesis. Cambridge, USA: Massachusetts Institute of Technology, 1979.

[142] Feng YR, Gong HY, Zhang YJ, *et al*. Effect of BN content on the mechanical and dielectric properties of porous BN_p/Si_3N_4 ceramics. *Ceram Int* 2016, **42**: 661–665.

[143] Liang GD, Bi JQ, Sun GX, *et al*. Effect of boron nitride nanosheets addition on the mechanical and dielectric properties of magnesium oxide ceramics. *Ceram Int* 2020, **46**: 23669–23676.

[144] Yang P, Wang LX, Zhao WH, *et al*. Hot-pressing sintered AlN–BN ceramics with high thermal conductivity and low dielectric loss. *Ceram Int* 2020, **46**: 8431–8437.

[145] Barick P, Saha BP. Effect of boron nitride addition on densification, microstructure, mechanical, thermal, and dielectric properties of β-SiAlON ceramic. *J Mater Eng Perform* 2021, **30**: 3603–3611.

[146] Weibull W. A statistical distribution function of wide applicability. *J Appl Mech* 2021, **18**: 293–297.

[147] Nie GL, Li YH, Sheng PF, *et al*. Microstructure refinement-homogenization and flexural strength improvement of Al_2O_3 ceramics fabricated by DLP-stereolithography integrated with chemical precipitation coating process. *J Adv Ceram* 2021, **10**: 790–808.

[148] Gong JH. A new probability index for estimating Weibull modulus for ceramics with the least-square method. *J Mater Sci Lett* 2000, **19**: 827–829.

[149] Deng B, Jiang DY, Gong JH. Is a three-parameter Weibull function really necessary for the characterization of the statistical variation of the strength of brittle ceramics? *J Eur Ceram Soc* 2018, **38**: 2234–2242.

[150] Weeks WP, Flores KM. Improving the precision of Vickers indentation measurements in soda-lime glass with increased dwell time. *J Non-Cryst Solids* 2023, **605**: 122174.

[151] Quinn G. Advanced structural ceramics: A round robin. *J Am Ceram Soc* 1990, **73**: 2374–2384.

[152] Alford NM, Birchall JD, Kendall K. Engineering ceramics—The process problem. *Mater Sci Technol* 1986, **2**: 329–336.

[153] Ono K. A simple estimation method of Weibull modulus and verification with strength data. *Appl Sci* 2019, **9**: 1575.

[154] Lu C. A reassessment of the strength distributions of advanced ceramics. *J Aust Ceram Soc* 2008, **44**: 38–41.

[155] Quinn JB, Quinn GD. A practical and systematic review of Weibull statistics for reporting strengths of dental materials. *Dent Mater* 2010, **26**: 135–147.

[156] Sun BA, Wang WH. The fracture of bulk metallic glasses. *Prog Mater Sci* 2015, **74**: 211–307.

[157] Gao CH, Proudhon H, Liu M. Three-dimensional finite element analysis of shallow indentation of rough strain-hardening surface. *Friction* 2019, **7**: 587–602.

[158] Andersson H. Analysis of a model for void growth and coalescence ahead of a moving crack tip. *J Mech Phys Solids* 1977, **25**: 217–233.

[159] Lee JS, Jang JI, Lee BW, *et al*. An instrumented indentation technique for estimating fracture toughness of ductile materials: A critical indentation energy model based on continuum damage mechanics. *Acta Mater* 2006, **54**: 1101–1109.

[160] Guan PF, Lu S, Spector MJB, *et al*. Cavitation in amorphous solids. *Phys Rev Lett* 2013, **110**: 185502.

[161] Gupta I, Sondergeld C, Rai C. Fracture toughness in shales using nano-indentation. *J Petrol Sci Eng* 2020, **191**: 107222.

[162] Liu M, Yang SH, Gao CH. Scratch behavior of polycarbonate by Rockwell C diamond indenter under progressive loading. *Polym Test* 2020, **90**: 106643.

[163] Liu M. Microscratch of copper by a Rockwell C diamond indenter under a constant. *Nanotechnol Precis Eng* 2021, **4**: 033003.

[164] Liu M, Wu JN, Gao CH. Sliding of a diamond sphere on K9 glass under progressive load. *J Non-Cryst Solids* 2019, **526**: 119711.

[165] Parvin M, Williams JG. Ductile–brittle fracture transitions in polycarbonate. *Int J Fract* 1975, **11**: 963–972.

[166] Liu M, Wu JN. Scratch behavior of materials under progressive load by conical indenter. *Chinese J Mater Res* 2022, **36**: 191–205. (in Chinese)